Ph. D. DISSERTATION

Top-down Design of Reconfigurable Bianisotropic Acoustic Metamaterials beyond the Passivity and Reciprocity

수동성 및 호혜성 한계를 극복하는 가변형 쌍이방성 음향 메타물질의 하향 설계

BY

CHOONLAE CHO

FEBRUARY 2021

DEPARTMENT OF ELECTRICAL ENGINEERING AND COMPUTER SCIENCE
COLLEGE OF ENGINEERING
SEOUL NATIONAL UNIVERSITY

Top-down Design of Reconfigurable Bianisotropic Acoustic Metamaterials |beyond the Passivity and Reciprocity

수동성 및 호혜성 한계를 극복하는 가변형 쌍이방성 음향 메타물질의 하향 설계

지도 교수 박 남 규

이 논문을 공학박사 학위논문으로 제출함

2021 년 2 월

서울대학교 대학원

전기·컴퓨터 공학부

조 춘 래

조춘래의 공학박사 학위논문을 인준함

2021 년 2 월

위 원 장 이 병 호 (인)

부위원장 박 남 규 (인)

위 원 정 윤 찬 (인)

위 원 민 범 기 (인)

위 원 노 준 석 (인)

Abstract

Top-down Design of Reconfigurable Bianisotropic Acoustic Metamaterials beyond the Passivity and Reciprocity

CHOONLAE CHO
DEPARTMENT OF ELECTRICAL ENGINEERING AND COMPUTER SCIENCE
COLLEGE OF ENGINEERING
SEOUL NATIONAL UNIVERSITY

Over the past two decades, metamaterials have revolutionized how we manipulate classical waves. They allow us to obtain constitutive parameters beyond the bound of natural materials by artificially designing tailor-made resonance modes in the unit structure. Since all wave dynamics are anticipated from the constitutive parameters landscape in which the wave propagates, the implementation of entire constitutive parameters enables intriguing theoretical and practical applications in many wave systems, such as negative refraction and invisibility cloaking. Although various structures have been successfully proposed to obtain extraordinary wave properties, the

design approach to the existing metamaterial poses fundamental challenges in realizing the physical properties.

In many practical applications, metamaterial structures capable of independent control of each wave property has been envisaged as an ideal platform for reconfigurability. While metamaterial structures consisting of a combined substructure that controls one of the fundamental resonances have been proposed, it is required that an integrated platform offering decoupled control of the wave parameters. In particular, in the case of reconfigurable metamaterials, tuning the constitutive parameters depends on modifying the physical structure attached to the metamaterials, posing a fundamental challenge in the tuning range. Therefore, there is a need for a study to achieve flexible control and realize extreme properties.

In this dissertation, I provide the top-down design approach of the reconfigurable acoustic metamaterial that overcomes conventional limitations and achieves designer wave properties. Based on the principles of decoupling of fundamental resonances, acoustic metamaterial platforms that offer independent control of wave parameters and their applications are presented. Then, I propose the concept of virtualized metamaterials on their signal response function to escape the boundary inherent in the physical structure of metamaterials, which generate artificial polarizations based on the digital signal processing technique, escaping physically resonating structure. Virtualized metamaterials enable decoupled control of all possible complex wave parameters in a reconfigurable manner and extreme wave

properties. This dissertation is expected to provide a breakthrough in metamaterial design by implementing all wave properties independently, realizing designable frequency dispersion characteristics, and providing a flexible platform that can realize acoustic metamaterials' full capability.

Keywords : Metamaterials, Acoustics, Bianisotropy, Active Metamaterials, Wave dynamics

Student Number : 2013-20890

Table of Contents

List of Figures

Chapter 1

Introduction

In this chapter, I overview the progress and challenges in metamaterials. I introduce metamaterials in electromagnetic, acoustic, and elastic systems and present practical applications in a sense manipulating wave dynamics. Recent achievements and fundamental challenges underlying in realize metamaterials are discussed. In the last part, the scope and outline of this dissertation are described.

1.1. Achievements and challenges in metamaterials

Metamaterials are artificial structures that offer extraordinary wave properties that cannot found in natural media. They enable unusual manipulations of classical waves, initially in the case of electromagnetic waves [1-9] and subsequently for acoustic waves [10-18], water waves[19], and more recently, elastic waves in solids [20-24]. In electromagnetics, artificial magnetism exhibiting negative permeability [5], double negative metamaterials [6], matched-zero index materials [7,8], and extremely high index metamaterials [9] have been demonstrated in microwave, terahertz, and optical frequencies. With a similar analogy to the electromagnetic metamaterials, acoustic and elastic metamaterials have realized tailor-made resonances for bulk modulus [12] and mass density [14] in different frequencies and background systems. The ability of metamaterials to acquire physical properties beyond those of natural materials reflects the engineering degrees of freedom in designing artificial structures.

Since then, many intriguing phenomena manipulating classical waves further than the conventional method have been demonstrated, such as negative refraction [25-27], superfocusing [28-32], extraordinary transmission [33], invisibility cloaking [34-36], and metasurfaces [37-39]. In addition, metamaterials allow the quantum-classical analogy [40], which enables not only the classical simulation of unstable quantum phenomena [41,42] but also quantized wave dynamics in the classical system, including the quantum Hall effect and topological theory [43-46], parity-time symmetry and non-Hermitian degeneracy [47], Anderson localization [48], Bloch oscillations [49,50], and supersymmetry [51-55], which require the most extreme values of the constitutive parameters [56,57]. These effects consistently confirm that metamaterials can be designed to yield a wide range of constitutive parameters and can be inhomogeneous.

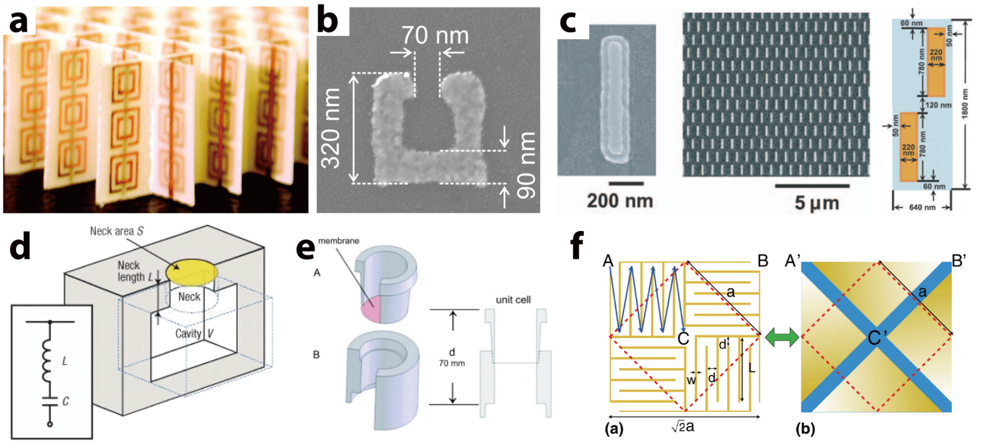

Figure 1.1 | **a-c**, Electromagnetic metamaterials exhibiting artificial magnetism. (**a**) Photograph of the zero-index metamaterial sample consists of SRR and wire strips at microwave [3]. (**b**) An electron micrograph of an SRR fabricated by electron-beam lithography for 100 THz [5]. (**c**) Field-emission scanning electron microscope images (left) and elementary cell (right) of optical negative index metamaterial [6]. **d-f**, Acoustic metamaterials (**d**) Helmholtz resonator with negative bulk modulus [12]. (**e**) Membrane type acoustic metamaterials with negative mass density [14]. (**f**) Negative refractive index using space-coiling structure [16].

To make further use of metamaterials in practical situations, many applications require tunability or reconfigurability. This can be achieved by optical pumping active materials [58,59], mechanically changing geometric parameters using MEMS [60,61], or combining external RLC circuit elements with metamaterial structures. Tuning can also be extended to the level of each atom when backend electronics such as an FPGA chip or a computer are used to store and alter the state of the controlling parameters [62-64]. For most of these metamaterials, the tuning largely depends on the actual mechanism for modifying the metamaterial resonance of the physical structures.

To this end, the separation of wave parameters has been predicted as an ideal platform for the deterministic reconfiguration of the meta-atom [65], while its validity has not yet responded. In many cases, metamaterial design has been realized using bottom-up, retro-fit approaches, in which the building blocks are proposed first, and the subsequent design is performed through a series of iterations and guesswork. Furthermore, reconfigurable metamaterials pose a fundamental challenge in terms of the degree of flexibility or range of tunability, which is crucial in many applications requiring real-time reconfigurability. Additionally, it is hard to imagine using standard approaches for separately configuring resonating strength, bandwidth, and phase lag, e.g., for a Lorentzian frequency dispersion, as these depend on the actual tuning mechanisms.

In the context of tunability and reconfigurability, acoustic metamaterials, mainly programmable by electronically controlled elements, can be used to achieve a wide range of tunable effective parameters [66-70]. These acoustic metamaterials have proved useful as a platform for many intriguing wave phenomena, such as unidirectional invisibility [67], sound isolation [68], Willis coupling [69], and highly tunable mechanical properties [70]. These works point to the direction that programmable control with external circuits or microprocessors can be used to provide a higher level of abstraction of the physical properties of metamaterials.

1.2. Outline of the dissertation

This dissertation is focused on the design of bianisotropic acoustic metamaterial to provide a platform that enables decoupled control of acoustic wave properties in a reconfigurable way, as well as to offer extreme wave properties.

In chapter 2, I introduce acoustic wave dynamics starting from the duality relation between acoustics and electromagnetics. Then I provide the definition and characteristics of bianisotropy and its applications. The experimental methods utilized in this work are also elaborated here. In chapter 3, the top-down approach of bianisotropic acoustic metamaterials is addressed, and meta-atom structures implemented with membrane and space-coiling structures are provided. By extending the generalized Snell's law, it is also introduced that deterministic approach to design metasurface, which independently manipulates reflection and transmission wavefronts. Chapter 4 present the concept of virtualized metamaterials, reconfigurable metamaterials that generate artificial polarization based on the digital convolution signal processing technique. Demonstration of one-dimensional acoustic virtualized meta-atom proved programmable polarizabilities in a top-down manner. In chapter 5, by extending the virtualization concept to bianisotropic metamaterials, extreme wave properties including reciprocal bianisotropy beyond the passivity limit, remarkably high nonreciprocity without rapid flow, and broadband-, flat- frequency dispersions are demonstrated.

Chapter 2

Acoustic Wave Dynamics

This chapter introduces the background theory of linear acoustic wave dynamics. First, I briefly provide the governing wave equations for acoustic and electromagnetic systems, focusing on the duality relationship. The characteristics of bianisotropy with detailed classification are discussed in the electromagnetic and acoustic domains. Finally, experimental methods for the bianisotropic acoustic medium utilized in this work are described.

2.1 Duality relation between acoustics and electromagnetics

The similarity between governing equations in different physical systems has provided novel perspectives and applications distinct from traditional viewpoints. This section provides the duality relation between acoustics and electromagnetics. Acoustic wave dynamics are governed by the linearized Euler's equations consist of conservation of mass and Newton's second law,

$$\begin{aligned} \nabla p &= -\partial_t \boldsymbol{\pi}, \\ \nabla \cdot \mathbf{v} &= -\partial_t e, \end{aligned} \tag{2.1}$$

where p and $\mathbf{v}$ are acoustic pressure and velocity fields, $\boldsymbol{\pi}$ is the momentum field, and e is the strain field. In isotropic acoustic media, strain and momentum fields are simply defined as

$$\begin{aligned} e &= B^{-1} p, \\ \boldsymbol{\pi} &= \rho \mathbf{v}, \end{aligned} \tag{2.2}$$

where B is the bulk modulus and ρ is the mass density. Eqs. (2.1) and (2.2) lead to the acoustic wave equation for the scalar pressure field as

$$\nabla^2 p - \frac{1}{c^2} \partial_t^{\,2} p = 0, \tag{2.3}$$

or equivalently, but for the velocity field,

$$\nabla^2 \mathbf{v} - \frac{1}{c^2} \partial_t^{\,2} \mathbf{v} = 0, \tag{2.4}$$

where $c = (B/\rho)^{1/2}$ is the speed of the acoustic wave.

On the other hand, electromagnetic wave dynamics are governed by the Maxwell equations, of which source-free case can be written as,

$$\begin{aligned} \nabla \times \mathbf{E} &= -\partial_t \mathbf{B} \\ \nabla \times \mathbf{H} &= \partial_t \mathbf{D} \\ \nabla \cdot \mathbf{D} &= 0 \\ \nabla \cdot \mathbf{B} &= 0 \end{aligned} \tag{2.5}$$

where **E**, **H**, **D**, and **B** are electric field, magnetic field, electric displacement, and magnetic field density, respectively, with constitutive relation

$$\begin{aligned} \mathbf{D} &= \varepsilon \mathbf{E} \\ \mathbf{B} &= \mu \mathbf{H} \end{aligned} \tag{2.6}$$

where ε and μ are electric permittivity and magnetic permeability. These two equations have a duality relation between two-dimensional acoustic and electromagnetic systems with a single polarization. In Cartesian coordinate, the acoustic wave and transverse electric (TE) or transverse magnetic (TM) polarized electromagnetic waves which only contain z-directional electric field $\mathbf{E} = E_z\mathbf{z}$ or $\mathbf{H} = H_z\mathbf{z}$ are identical when exchanging the variables as follows:

$$\text{TE case } \begin{bmatrix} p & \mathbf{v} & B^{-1} & \rho \end{bmatrix} \Leftrightarrow \begin{bmatrix} E_z & \mathbf{z}\times\mathbf{H} & \varepsilon & \mu \end{bmatrix}, \tag{2.7a}$$

$$\text{TM case } \begin{bmatrix} p & \mathbf{v} & B^{-1} & \rho \end{bmatrix} \Leftrightarrow \begin{bmatrix} H_z & -\mathbf{z}\times\mathbf{E} & \mu & \varepsilon \end{bmatrix}. \tag{2.7b}$$

While acoustic wave equations do not satisfy invariant symmetry in 3D [71], which is crucial for the coordinate transformation[65], duality relations in Eq. (2.7) enable direct adaption of electromagnetically demonstrated phenomena into acoustic systems, e.g., acoustic cloaking [72-74], acoustic hyperlens [75], extraordinary acoustic transmission [76], and many intriguing applications. It is noted that because acoustic waves with a solely longitudinal nature offer a single polarization mode, duality relation cannot be utilized for electromagnetic waves with mixed polarization. I further note that the elastic waves that have both longitudinal and transverse polarizations can have a duality relation with the electromagnetic system while it requires polarization restrictions in elastic systems.

2.2 Bianisotropy

2.2.1 Bianisotropy in electromagnetics

Bianisotropy is an exotic electromagnetic property that describes the coupling between electric and magnetic fields. The simplest form of electric and magnetic field coupling, which is referred to as bi-isotropy, can be expressed by the following constitutive relation,

$$\begin{aligned}\mathbf{D} &= \varepsilon\mathbf{E} + \xi\mathbf{H} \\ \mathbf{B} &= \mu\mathbf{H} + \zeta\mathbf{E}\end{aligned} \tag{2.8}$$

where ξ and ζ are magnetoelectric- and electromagnetic- coupling constants, or simply bi-isotropic parameters. By decomposing ξ and ζ based on the Lorentz reciprocity, Eq. (2.8) can be rewritten as,

$$\begin{aligned}\mathbf{D} &= \varepsilon\mathbf{E} + (\chi - i\kappa)\mathbf{H} \\ \mathbf{B} &= \mu\mathbf{H} + (\chi + i\kappa)\mathbf{E}\end{aligned} \tag{2.9}$$

where $\kappa \equiv i(\xi - \zeta)/2$ and $\chi \equiv i(\xi + \zeta)/2$ are reciprocal- and nonreciprocal bi-isotropic parameter, respectively. In bi-isotropic materials for both reciprocal and nonreciprocal cases, the cross-coupling results in energy exchange between different polarizations, and thus, waves propagating in these media undergo polarization rotation. Bi-isotropic reciprocal media ($\kappa \neq 0$) is often referred to as chiral media, while the bi-isotropic nonreciprocal media ($\chi \neq 0$) is called Tellegen media [77], which has long been debated whether they can physically realizable.

To further generalize bi-isotropy, one can conceive cross-coupling with anisotropic tensorial form as anisotropic media. These generalized linear electromagnetic properties can be written as following bianisotropic constitutive relations

$$\begin{aligned}\mathbf{D} &= \boldsymbol{\varepsilon}\cdot\mathbf{E}+\boldsymbol{\xi}\cdot\mathbf{H}\\ \mathbf{B} &= \boldsymbol{\mu}\cdot\mathbf{H}+\boldsymbol{\zeta}\cdot\mathbf{E}\end{aligned} \tag{2.10}$$

where $\boldsymbol{\varepsilon}$ and $\boldsymbol{\mu}$ are the permittivity and permeability parameters in the form of dyadic tensor, $\boldsymbol{\xi}$ and $\boldsymbol{\zeta}$ are bianisotropic dyadic. Again based on the Lorentz reciprocity, Eq. (2.10) can be rewritten as,

$$\begin{aligned}\mathbf{D} &= \boldsymbol{\varepsilon}\cdot\mathbf{E}+\left(\boldsymbol{\chi}^{T}-i\boldsymbol{\kappa}^{T}\right)\cdot\mathbf{H}\\ \mathbf{B} &= \boldsymbol{\mu}\cdot\mathbf{H}+\left(\boldsymbol{\chi}+i\boldsymbol{\kappa}\right)\cdot\mathbf{E}\end{aligned} \tag{2.11}$$

where $\boldsymbol{\kappa} \equiv i(\boldsymbol{\xi}^{T} - \boldsymbol{\zeta})/2$ and $\boldsymbol{\chi} \equiv i(\boldsymbol{\xi}^{T} + \boldsymbol{\zeta})/2$ are reciprocal- and nonreciprocal-bianisotropic parameters, respectively, with superscript T denotes transpose operation.

The bianisotropy can be classified into two significant groups based on the symmetry of the bianisotropic dyadic. First, the media with symmetric $\boldsymbol{\kappa}$ and $\boldsymbol{\chi}$, i.e., $\boldsymbol{\kappa} = \boldsymbol{\kappa}^{T}$ and $\boldsymbol{\chi} = \boldsymbol{\chi}^{T}$, are usually referred to as bi-isotropic since these kinds of couplings involve energy exchange between different polarizations as bi-isotropic media discussed above. On the other hand, antisymmetric $\boldsymbol{\kappa}$ and $\boldsymbol{\chi}$, i.e., $\boldsymbol{\kappa} = -\boldsymbol{\kappa}^{T}$ and $\boldsymbol{\chi} = -\boldsymbol{\chi}^{T}$ are called bianisotropic parameters, distinguished by their unique property that exchanges the intensity between electric and magnetic field in the same polarization. More strict classification and capabilities of the bianisotropy can be found in Tretyakov et al. [78].

Media with antisymmetric **κ** will exchange the intensity between electric and magnetic fields while conserving the polarization. These media are called omega media since Ω-shape structure can efficiently produce electromagnetic coupling in a single polarization. In omega media, wave feels different impedances depending on the direction of propagation. For example, in one-dimensional reciprocal bianisotropic media with

$$\boldsymbol{\varepsilon} = \varepsilon \mathbf{I},\ \boldsymbol{\mu} = \mu \mathbf{I},\ \boldsymbol{\kappa} = \begin{pmatrix} 0 & 0 & 0 \\ 0 & 0 & 0 \\ 0 & \kappa & 0 \end{pmatrix}, \tag{2.12}$$

where **I** is the unit dyadic, wave impedances for $+x$ and $-x$ directions are given by

$$z_f = \frac{\mu}{n + i\kappa}, \qquad z_b = \frac{\mu}{n - i\kappa}, \tag{2.13}$$

with refractive index $n = \pm(\varepsilon\mu - \kappa^2)^{1/2}$.

Antisymmetric **χ**, i.e., nonreciprocal bianisotropy, has a close relationship to the Lorentz transformation of moving media. i.e., objects moving with the velocity **v** feels bianisotropic parameter as

$$\chi_{ij} = -\frac{n^2 - 1}{1 - n^2\beta^2}\varepsilon_{ijk}\beta_k, \tag{2.14}$$

where $\boldsymbol{\beta}$ = $\mathbf{v}/c_0$, n is the refractive index of the reference media. In the nonreciprocal bianisotropic media, the wave feels a different refractive index along the propagation direction. In a 1-D system with

$$\boldsymbol{\varepsilon} = \varepsilon\mathbf{I},\ \boldsymbol{\mu} = \mu\mathbf{I},\ \boldsymbol{\chi} = \begin{pmatrix} 0 & 0 & 0 \\ 0 & 0 & 0 \\ 0 & \chi & 0 \end{pmatrix}, \tag{2.15}$$

refractive indices for $+x$ and $-x$ directions are given by

$$n_f = n - \chi, \qquad n_b = n + \chi, \tag{2.16}$$

where n is the refractive index of the reference media.

It is important to investigate the scattering properties of a bianisotropic slab for applications such as bianisotropic metasurface. For the reciprocal bianisotropic case, reflection coefficients could differ because of the directional impedances, while the transmittance should be identical. On the other hand, for the nonreciprocal bianisotropy, the transmittance is different by the different refractive index, while reflection coefficients are the same. I further generalize the above direction-wise scattering parameters in one-dimensional bianisotropic media. When the wave propagates through the bianisotropic slab with thickness d and wave parameters,

$$\boldsymbol{\varepsilon} = \varepsilon\mathbf{I},\ \boldsymbol{\mu} = \mu\mathbf{I},\ \boldsymbol{\kappa} = \begin{pmatrix} 0 & 0 & 0 \\ 0 & 0 & 0 \\ 0 & \kappa & 0 \end{pmatrix},\ \boldsymbol{\chi} = \begin{pmatrix} 0 & 0 & 0 \\ 0 & 0 & 0 \\ 0 & \chi & 0 \end{pmatrix}, \tag{2.17}$$

scattering parameters (S-parameters) are given by

$$\begin{aligned}
S_{11} &= \frac{2i\mu\left(\varepsilon-\mu+2i\kappa\right)\sin\left(nk_0 d\right)}{\left(2n+\left(\mu+\varepsilon\right)\right)e^{-ink_0 d}+\left(2n-\left(\mu+\varepsilon\right)\right)e^{ink_0 d}}, \\
S_{12} &= \frac{4ne^{in_b k_0 d}}{\left(2n+\left(\mu+\varepsilon\right)\right)e^{-ink_0 d}+\left(2n-\left(\mu+\varepsilon\right)\right)e^{ink_0 d}}, \\
S_{21} &= \frac{4ne^{in_f k_0 d}}{\left(2n+\left(\mu+\varepsilon\right)\right)e^{-ink_0 d}+\left(2n-\left(\mu+\varepsilon\right)\right)e^{ink_0 d}}, \\
S_{22} &= \frac{2i\mu\left(\varepsilon-\mu-2i\kappa\right)\sin\left(nk_0 d\right)}{\left(2n+\left(\mu+\varepsilon\right)\right)e^{-ink_0 d}+\left(2n-\left(\mu+\varepsilon\right)\right)e^{ink_0 d}}
\end{aligned} \tag{2.18}$$

with direction-wise refractive indices and impedances in Eqs. (2.13) and (2.16). While in mirror-symmetric metamaterials which are non-bianisotropic, S-parameters are simply represented by reflection coefficient S_{11} = S_{22} and transmission coefficient S_{21} = S_{12}, all four S-parameters have to be elaborated in bianisotropic media to extract wave parameters accurately.

2.2.2 Acoustic bianisotropy

There exist an acoustic analogy of bianisotropy that describes the coupling between pressure and velocity field. Acoustic bianisotropy, also known as the acoustic Willis coupling, was originally anticipated by Willis et al. [79] in elastic waves. In bianisotropic acoustic media, constitutive relations are given by

$$\begin{aligned} e &= B^{-1} p + \left(\boldsymbol{\chi}^T - i\boldsymbol{\kappa}^T\right)\cdot \mathbf{v} \\ \boldsymbol{\pi} &= \boldsymbol{\rho}\cdot \mathbf{v} + \left(\boldsymbol{\chi} + i\boldsymbol{\kappa}\right) p \end{aligned} \tag{2.19}$$

where $\boldsymbol{\rho}$ is the mass density dyadic tensor and $\boldsymbol{\kappa}$ and $\boldsymbol{\chi}$ are reciprocal and nonreciprocal bianisotropic parameters, respectively, which are the first order dyadic. It is noted that as implicitly described in Eq. (2.19), due to the longitudinal nature of acoustic waves, acoustic bianisotropy must not be bi-isotropic but bianisotropic. Therefore, acoustic bianisotropic media have a duality relation with the electromagnetic system with specific single-polarization, and thus the characteristics are identical to the electromagnetic bianisotropic media such as omega media and moving media.

To realize acoustic bianisotropy, it is required to break the mirror symmetry as analogous to electromagnetic bianisotropy. Considering the wave longitudinal nature of the acoustic wave, the asymmetry along the acoustic wave propagation direction lifts the reciprocal bianisotropy like omega media. In Fig. 2.1, reciprocal bianisotropy is demonstrated by breaking the mirror symmetry: Demonstration of acoustic bianisotropy utilizes asymmetrically located resonating membranes along the propagation direction (Fig. 2.1a,b) [80,81]. By maximizing the asymmetry of the Helmholtz resonator, reciprocal bianisotropy close to the theoretical maximum was demonstrated (Fig. 2.1c) [82]

For the nonreciprocal bianisotropy, asymmetric flow cause the nonreciprocal bianisotropy along the current direction, which can be written as,

$$\chi = -\frac{M}{1-M^2}, \tag{2.20}$$

where $M = v/c_0$ is the Mach number, v is the flow speed, and c_0 is the speed of acoustic wave [83]. This result is similar to the Lorentz transformation in electromagnetics, while differences lie in the relativistic perspectives. Figure 2.2 shows examples of nonreciprocal acoustic bianisotropic media realized by circulating fluid [84] and deriving speakers [85].

The recent realization of acoustic bianisotropy with an adequately designed inverse bulk modulus and mass density enables the exotic manipulation of acoustic waves. Figure 2.3 shows applications of bianisotropic acoustic metamaterials. Reciprocal bianisotropic media allows acoustic metagratings that manipulate acoustic wavefront with single unit cell structure (Fig. 2.3a) [86] and diffraction free metasurface, which enables 100% transmission of power without diffraction losses (Fig. 2.3b) [87]. Nonreciprocal bianisotropic media realizes acoustic circulator, which is analogous to optical Zeeman effect (Fig. 2.3c) [84], and directional wave manipulations (Fig. 2.3d) [83].

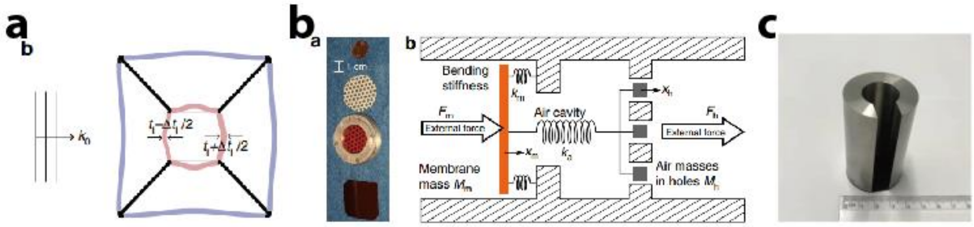

Figure 2.1 | Acoustic reciprocal bianisotropic metamaterials using **a**,**b,** asymmetric membranes [80,81] and **c,** Helmholtz resonator [82].

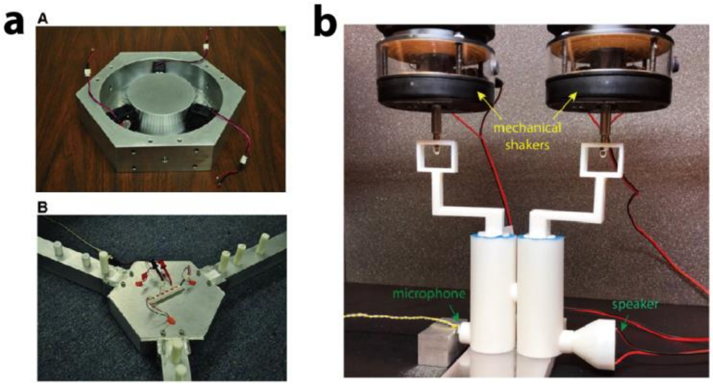

Figure 2.2 | Acoustic nonreciprocal bianisotropic metamaterials using **a**, circulating fluid [84], **b**, resonator cascaded deriving speakers [85].

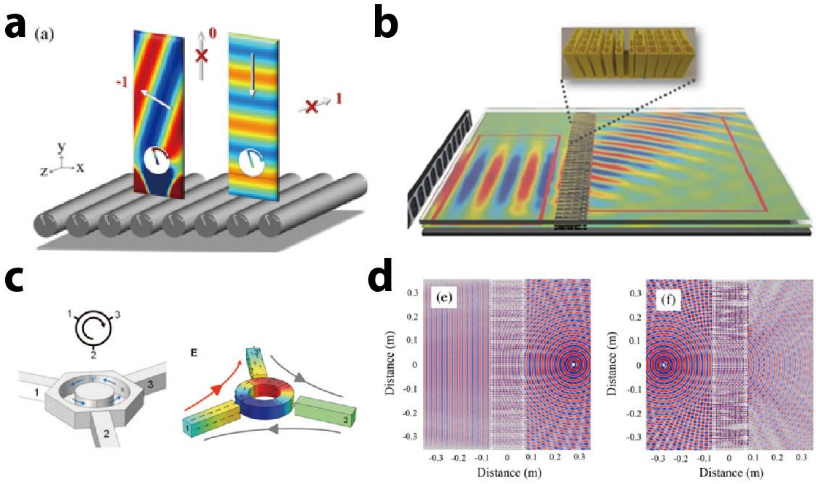

Figure 2.3 | Applications of acoustic bianisotropic metamaterials. **a**, Acoustic metagrating [86], **b**, diffraction free metasurface [87], **c,** Acoustic isolator [84], and **d**, nonreciprocal metalens [83].

2.3 Experimental methods

To characterize acoustic properties of metamaterials such as mass density, inverse bulk modulus, and bianisotropy, 4-point measurement with a National Instruments DAQ device and LabVIEW have been used with a properly designed impedance tube. The impedance tube, which is an acoustic waveguide with a small cross-section compared to the wavelength of interest to carry node-free one-dimensional acoustic waves, measures the specimen's scattering coefficients. As depicted in Fig. 2.4, the incident acoustic wave generated by the loudspeaker is scattered by the specimen, and four microphones - two of them are located on the upstream side, and the others are on the downstream side measure forward and backward propagating components at each side. Microphone detected signal can be expressed by

$$\begin{aligned}
p_{1+} &= \frac{M_1 e^{ikx_1} - M_2 e^{ikx_2}}{e^{2ikx_1} - e^{2ikx_2}}, \\
p_{1-} &= \frac{M_2 e^{ik(2x_1+x_2)} - M_1 e^{ik(x_1+2x_2)}}{e^{2ikx_1} - e^{2ikx_2}}, \\
p_{2+} &= \frac{M_3 e^{ikx_3} - M_4 e^{ikx_4}}{e^{2ikx_3} - e^{2ikx_4}}, \\
p_{2-} &= \frac{M_4 e^{ik(2x_3+x_4)} - M_3 e^{ik(x_3+2x_4)}}{e^{2ikx_3} - e^{2ikx_4}},
\end{aligned} \tag{2.21}$$

where M_1, M_2, M_3, and M_4 are microphone detected signal. The S-parameters of the specimen can then be given as follows.

$$\begin{pmatrix} p_{1-} \\ p_{2+} \end{pmatrix} = \begin{pmatrix} S_{11} & S_{12} \\ S_{21} & S_{22} \end{pmatrix} \begin{pmatrix} p_{1+} \\ p_{2-} \end{pmatrix}. \tag{2.20}$$

In non-bianisotropic media, the reciprocity constrains $S_{11} = S_{22}$ and $S_{12} = S_{21}$, and thus single measurement can determine S-parameters. However, bianisotropic media require at least two times measurements with independent incident waves. In this work, the scattering properties of the meta-atom were tested by means of incident waves coming from the forward and backward directions. In the experimental setup, I flipped the orientation of the meta-atom, while the waves were always incident from the same end of the impedance tube.

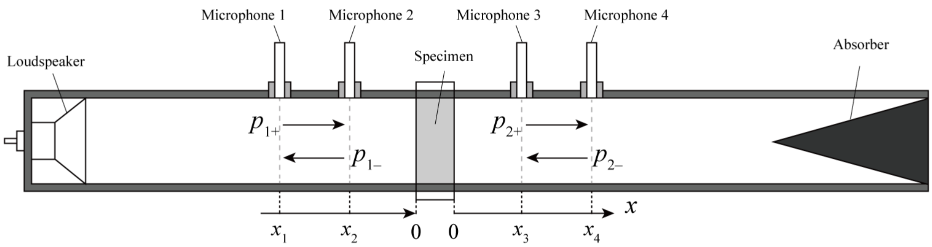

Figure 2.4 | Schematics of 4-point measurement method in an impedance tube.

Chapter 3

Top-down Design of Acoustic Metamaterials

In this chapter, I introduce the top-down design approach, the strategy for the decoupling of fundamental oscillations, which allows independent control of wave parameters. Based on the separation of characteristic oscillations, the underwater design of one-dimensional bianisotropic meta-atom controlling mass density, the inverse of bulk modulus, and bianisotropy near zero-index point is presented. I also propose bianisotropic acoustic metasurfaces that manipulate reflection and transmission wavefront independently by extending the concept of generalized Snell's law, which enables deterministic control of reflection and transmission coefficients. Lastly, I also present the design of two-dimensional acoustic metamaterials using a space-coiling structure that is readily applicable to other background acoustic media.

3.1 Introduction to a top-down approach to design metamaterials

For the reconfigurable control of metamaterials, independent and decoupled access to each wave properties are desired. To this end, metamaterials have been demonstrated that allow independent adjustment of each wave parameter [56,88-90], while most of them consist of substructures that adjust only one of the fundamental resonances responsible for the wave parameters. These fundamental oscillations are basically monopole and dipole resonance, which is elucidated from the effective medium theory for electromagnetics [91], the acoustics [80], or the elastics [92]. These can also be found in the Dirac-like point in zero-index metamaterials, where fundamental modes for each wave parameters degenerate. Figure 3.1 shows the dispersion relation of zero-index metamaterial and three eigenmodes at triply degenerated Dirac-like point of TE polarized electromagnetic waves in which permittivity and permeability are controlled by the monopolar and dipolar resonances. From this zero-index point, all signs of wave parameter space can be accessed by tuning these resonance modes.

Therefore, to realize decoupled access to the wave parameters, the top-down design approach conceives the Lieb lattice-like cross-shaped meta-atom structure as depicted in Fig.3.2a. The unit cell consists of one central resonator resonating at ω_1 and four side resonators resonating at ω_2. And the coupling between the center to side resonator and side to side resonators is given by κ_{12} and κ_{22}, respectively. Then, the coupled-mode equations of the Lieb-like system can be summarized to eigenvalue problems as below,

$$\begin{pmatrix} \omega_1 & i\kappa_{12} & i\kappa_{12} & i\kappa_{12} & i\kappa_{12} \\ -i\kappa_{12} & \omega_2 & i\kappa_{22} & 0 & 0 \\ -i\kappa_{12} & -i\kappa_{22} & \omega_2 & 0 & 0 \\ -i\kappa_{12} & 0 & 0 & \omega_2 & i\kappa_{22} \\ -i\kappa_{12} & 0 & 0 & -i\kappa_{22} & \omega_2 \end{pmatrix} \psi = \omega\psi \,. \tag{3.1}$$

Eq. (3.1) has monopolar eigenmode $\boldsymbol{\psi}_0$ and degenerate dipolar eigenmodes ψ_x and ψ_y as shown in Fig. 3.2b, with resonance frequencies of each eigenmodes ω_0, ω_x, and ω_y. The system requires to have proper resonance frequencies ω_1 and ω_2 and coupling constants κ_{12} and κ_{22}, such that $\omega_0 = \omega_{x,y}$, to realize the zero-index property. These physical parameters can be realized with a variety of structures. For example, top-down acoustic metamaterials based on the mass loaded membrane resonator enables decoupled access to the bulk modulus and mass density by tuning the membrane mass [80]. The top-down approach can be used for different background media or different systems.

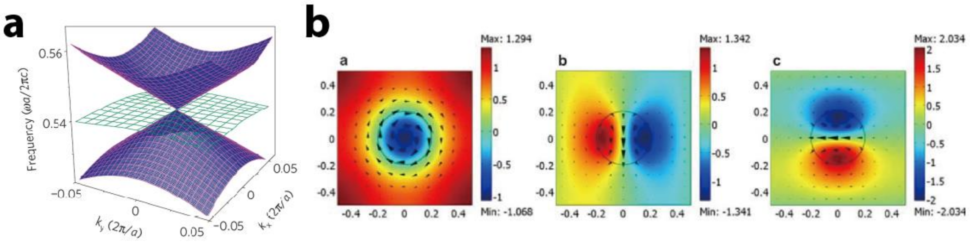

Figure 3.1 | Zero-index metamaterials and fundamental modes. **a,** Dirac-like dispersion near the zero-index frequency in the square lattice for TE electromagnetic waves. **b,** Fundamental modes at Dirac-like point for (left) *z*-directional permittivity and (mid and right) permeabilities for *y*- and *x*-directions [93].

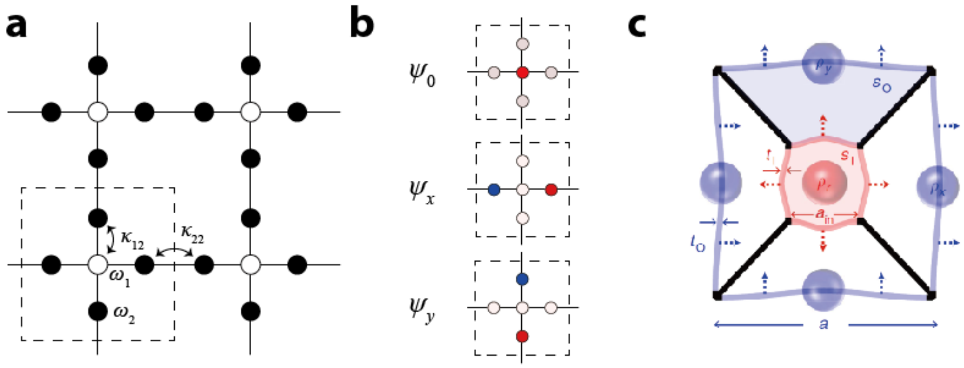

Figure 3.2 | Lieb-like structure and fundamental modes. **a**, Schematics of coupled-mode analysis to design zero-index metamaterials. **b**, Fundamental modes of interests. **c**, Implementation of top-down acoustic metamaterials based on the mass loaded membrane resonator [80].

3.2 Top-down design of bianisotropic acoustic metamaterials for underwater applications

In this section, I provide a 1-D top-down bianisotropic meta-atom design for underwater background media. In the water, the design of acoustic metamaterials suffers from the low contrast of inverse bulk modulus and mass density compare to that in the air. This limits the design degree of freedom by reducing the possibility of mass adjustment and increasing the complexity of the flexural stiffness of the membrane as a plate. Therefore, to utilize the same approach used in Ref. [80], I reduce the dimension of meta-atom to 1-D and use the membrane material like copper, which has a density of 8960 kg/m^3, due to the shortage of mass tunability as depicted in Fig.3.3a. In this structure, inverse bulk modulus, mass density, and bianisotropy are controlled by the thickness of the inner membrane t_i, outer membrane t_o, and the differences in inner membranes Δt_i. Figure 3.3b shows the frequency disperse on of the effective wave parameters retrieved from the S-parameters, which demonstrate the matched zero-index at a target frequency of 50 kHz when structural parameters of t_o = 2.2 mm and t_i = 1.5 mm. Here, solid lines and dashed lines are depicted with and without structural analysis, which includes the bending stiffness of the plate. In Fig. 3.3c-e, numerical analysis demonstrates the decoupled control of mass density, inverse bulk modulus, and bianisotropy with control parameters t_o, t_i, Δt_i, respectively.

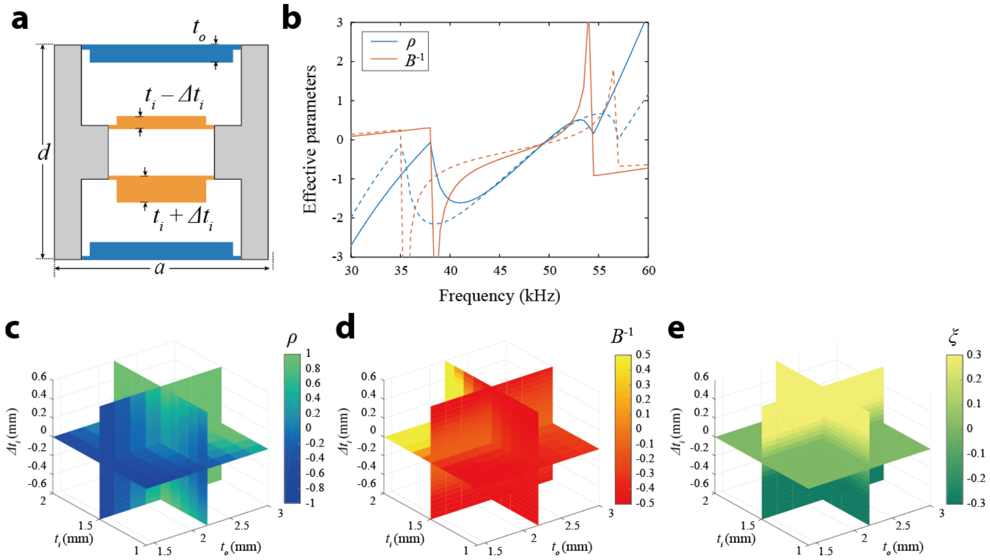

Figure 3.3 | 1-D acoustic metamaterials with resonating membrane for underwater operation. **a**, Schematics of designed acoustic meta-atom. Effective wave parameters mass density, inverse bulk modulus, and bianisotropy are controlled by the thickness of the inner membrane, outer membrane, and the differences in inner membranes. **b**, Frequency dispersion of effective wave parameters for matched zero-index meta-atom retrieved from scattering parameters. Solid lines and dashed lines are numerical calculations with and without structural analysis, which includes bending stiffness of the plate. **c-e**, Decoupled control of wave parameters in 1-D acoustic meta-atom. (**c**) Mass density, (**d**) inverse bulk modulus, and (**e**) reciprocal bianisotropy numerically obtained by the scattering parameter retrieval method.

3.3 Extended generalized Snell's law for independent manipulation of scattering wave-fronts

In this section, I propose bianisotropic acoustic metasurfaces that manipulate reflection and transmission wave-front independently. Metasurfaces enable compact wave manipulation by forming abrupt phase shifts within extremely thin thickness, where the phase shift is delicately designed to perform proper operations. For the manipulation of the wavefront, the generalized law of reflection and refraction is utilized, which is given by [37]

$$\begin{aligned} \sin(\theta_r) - \sin(\theta_i) &= \frac{\lambda_0}{2\pi n_i}\frac{d\Phi}{dx}, \\ \sin(\theta_t) n_t - \sin(\theta_i) n_i &= \frac{\lambda_0}{2\pi}\frac{d\Phi}{dx}. \end{aligned} \tag{3.2}$$

where θ_i, θ_r, and θ_t are the angle of incidence, target reflection, and transmission angle, n_i and n_t are the refractive indices in the incident and transmitted side media, λ_0 is the free space wavelength at operation frequency, and Φ is the required phase distribution on the metasurface. In this scheme, the phase shift is realized with the array of resonators that have an identical level of scattering amplitude but different phases covering all 2π range. In most cases, resonating structures are constructed by the bottom-up scenario, i.e., scanning the scattering amplitude and phase by sweeping structural parameters as shown in Fig. 3.4b,c.

For a more systematic manner, metasurfaces that controlling reflection and transmission wavefronts can be designed with the distribution of the bianisotropic wave parameters. For example, Huygens' surface [94] is the design approach based on the control of electric and magnetic polarizabilities to induce transmission phase shift while matching the impedances to make reflectionless metasurface. While the Huygens' surface can directly be used to control both wavefronts, it requires wave parameters of extremely high or non-passive values to cover all scattering range. Bianisotropic metasurface enables independent control of the reflection and transmission wave-front in a relived manner.

For the target complex reflection and transmission coefficients, required wave parameters are inversely calculated from Eq. (2.18). Figure 3.5 shows complex reflection and transmission coefficient mapped into the lossless, reciprocal bianisotropic parameters space for different amplitude ratios. It is noted that for the non-bianisotropic media, which correspond to the $\xi = 0$ surface in Fig. 3.5, extreme wave parameters away from the origin are required to cover the entire 2π phases of reflection and transmission. Utilizing bianisotropic meta-atom, we can deterministically design the metasurface demonstrating independent control of reflection and transmission wave.

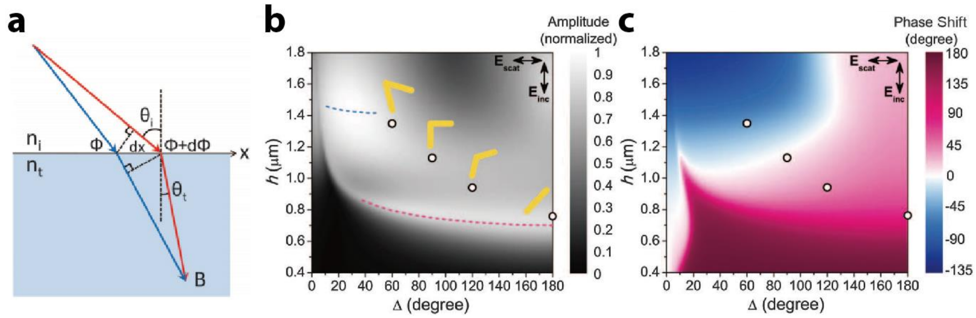

Figure 3.4 | Generalized law of reflection and refraction in a metasurface. **a**, The illustration of generalized law of refraction in case of abrupt phase shift on the surface. **b,c,** The scattering amplitude and phase of V-shaped nanoantenna.

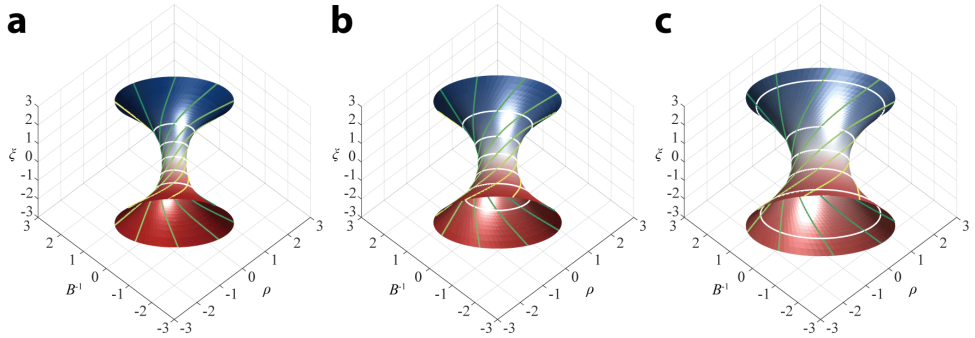

Figure 3.5 | Reflection and transmission phases on the iso-magnitude surface in bianisotropic parameter space. For three different intensity ratio R : T (**a**) 25% : 75%, (**b**) 50% : 50%, and (**c**) 75% : 25%, iso-phase contours (yellow to green for reflection and blue to red for transmission) are plotted on hyperbolic shaped iso-magnitude surface with the interval of π/4.

Figure 3.6 shows a numerical demonstration of a bianisotropic metasurface with selective control of reflection and/or transmission. The metasurface consists of a 48×1 array of meta-atoms and is designed to bend scattered waves with an intensity ratio between reflected and transmitted waves set to 25% : 75%. Required bianisotropic wave parameters are calculated inversely from the target phase of reflection and transmission coefficients in Fig. 3.6a. Figure 3.6b shows the scattered fields of each meta-atom that makes up the metasurfaces, showing clear agreement with target phases. In Fig. 3.6c, full-field simulations confirmed the operation of top-down bianisotropic metasurface with independent and deterministic control of the scattering wavefronts.

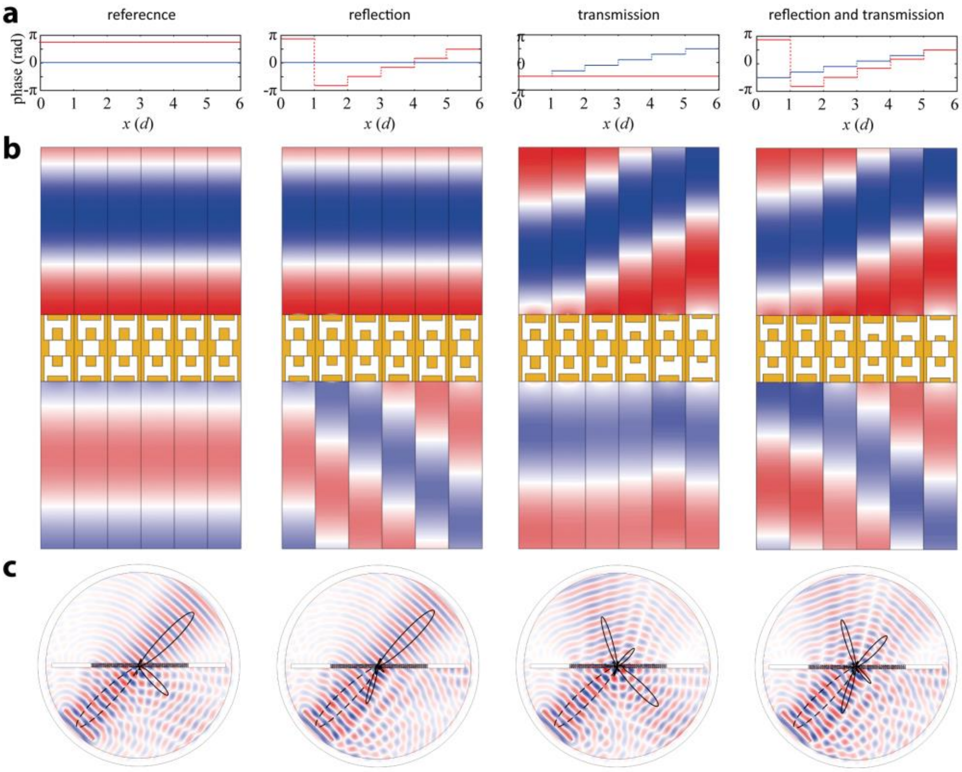

Figure 3.6 | Independent manipulation of reflection and/or transmission wavefronts in a bianisotropic metasurface. **a**, Target phase shift of each meta-atom. **b**, 1-D Scattered fields distribution of each meta-atom consisting metasurfaces. **c**, Full-wave simulation of the metasurface. Wave incidents from the bottom left with a 45° incident angle are reflected and scattered at the metasurfaces.

3.4 Space-coiling acoustic metamaterials for two-dimensional bianisotropic metamaterials

In this section, I provide the design of space-coiling type acoustic metamaterials enabling 2-D bianisotropy, readily scalable to the other system. The top-down design in section 3.1 requires control of coupling constants (membrane and mass) between the resonators (cells). To effectively tune the coupling constants, I adopt the space-coiling metamaterial structure that offers an extended path length to the system, which results in high effective mass. The proposed top-down metamaterial structure is depicted in Fig. 3.7a: external four cells and inner cells are connected with the meander structure, which is characterized by effective width w and path length l. For the system symmetry and design feasibility, space-coiling structures are split into n_s paths and n_f-times folded, which make effective path length to be $l = nd$. In this structure, wave parameters mass density, inverse bulk modulus, and bianisotropy are independently controlled by outer path depth $d_\mathrm{o} = f_\mathrm{o}d_{\mathrm{o}0}$, inner path depth $d_\mathrm{i} = f_\mathrm{i}d_{\mathrm{i}0}$, and the asymmetry of inner path depth $d_{\mathrm{i}\pm} = f_\mathrm{i}(1 + f_{\Delta\mathrm{i}})d_{\mathrm{i}0}$, where $d_{\mathrm{o}0}$ and $d_{\mathrm{o}0}$ are inner depth and outer depth of the zero index point, f_o, f_i, and $f_{\Delta\mathrm{i}}$ are tuning parameters. Figure 3.7b,c depicts numerically demonstrated zero-index acoustic metamaterials. In Fig. 3.7b, frequency dispersion of mass density and inverse bulk modulus matched zero index point at frequency 2950 Hz. Figure 3.7c shows 2-D Dirac-like ω–k dispersion relations near the zero-index point. The Dirac-like point is the signature of the zero index media where all three possible eigenmodes are degenerate at a specific frequency. The design parameters of a = 27.5 mm, w_o = 1 mm, w_i = 0.25 mm, and w_Δ = 0 are used in Fig. 3.7b,c. It is noted that zero-index frequencies in Fig. 3.7b,c are different because the numerical method utilized in Fig. 3.7b is wave parameter retrieval from scattering parameters, which integrate surface effects at the interface between the metamaterial and background media, on the other hand, Fig. 3.7c is obtained from eigenmode analysis assuming perfect periodicity. Figure 3.7d-f shows the decoupled control of wave parameters in the space-coiling structure. From the zero index point, tuning the control parameters f_o, f_i, and $f_{\Delta i}$ mostly control mass density, inverse bulk modulus, and bianisotropy. As space coiling metamaterials provide effective properties by not the material property but the structure geometry, metamaterials with the meander structure can directly be scaled to the other system, e.g., different frequencies and other background media. For example, the proposed space-coiling metamaterial structure here with a = 0.275 mm = 0.24 λ at 3 kHz in the air, can be used underwater at 5 kHz by scaling to a = 7.2 mm, which again corresponds to 0.24 λ.

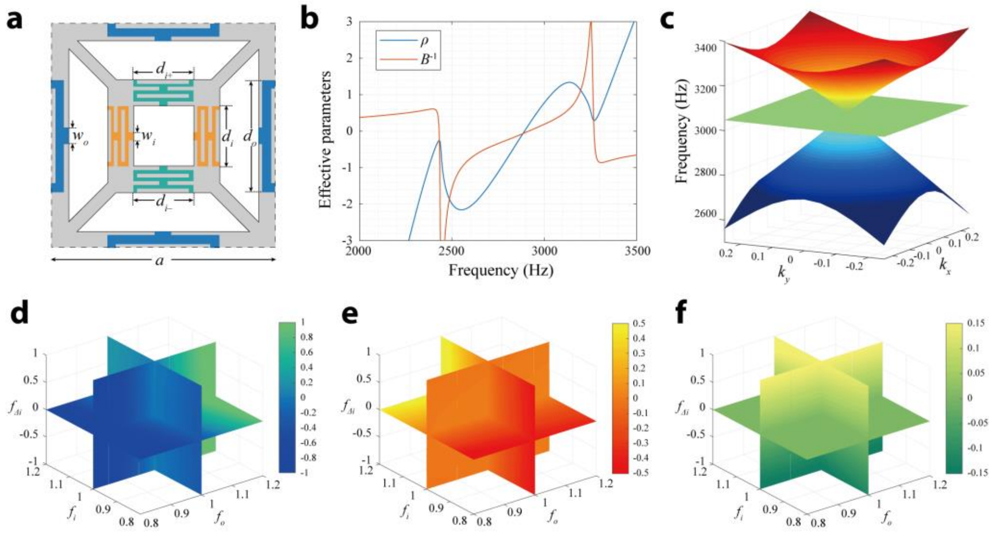

Figure 3.7 | Space-coiling top-down acoustic metamaterials. **a**, Schematics of designed space-coiling acoustic metamaterials. **b**, Numerically retrieved frequency dispersion of wave parameters. **c**, Dirac-like dispersion with triply-degeneracy of zero-index media. **d**-**f**, Decoupled control of wave parameters in space coiling acoustic metamaterials. (**d**) Mass density, (**e**) inverse bulk modulus, and (**f**) reciprocal bianisotropy numerically obtained by the scattering parameter retrieval method. Each wave parameter is solely controlled by the width of the outer path and inner path, and asymmetry of inner path width.

Figure 3.8 shows the plane wave propagation through the zero index metamaterials designed with space-coiling metamaterials. Metamaterials are composed of 5 × 10 arrays of matched zero index meta-atoms deigned in Fig. 3.7 and plane waves incident from bottom to top direction. In Fig. 3.8a, reflections occur at the incident interface because of the finite length of the slab, breaking the periodicity and induces local effects as mentioned above. In Fig. 3.8b,c, design modification in outermost atoms in first and fifth rows compensate the surface effects, showing clear scattering-free and zero phase shift propagation, even under the arbitrary defects inside.

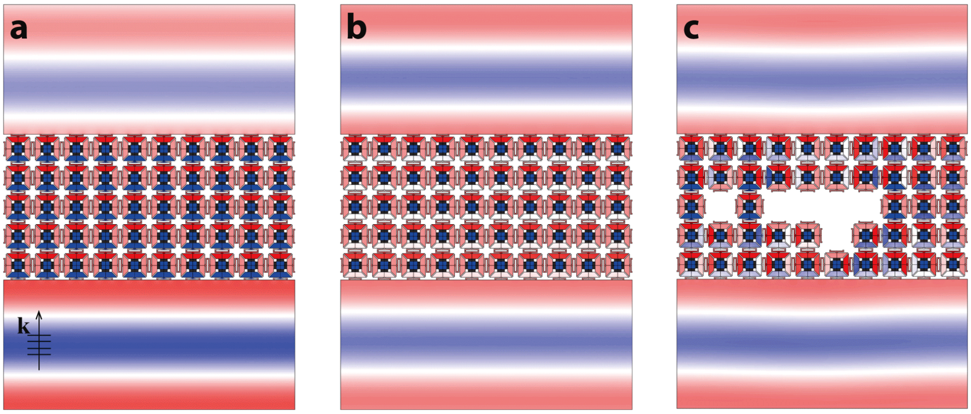

Figure 3.8 | Wave propagation through the matched zero-index metamaterials. **a**, Metamaterial composed of an array of matched zero index meta-atoms utilized in Fig. 3.1c. **b**, Metamaterial compensating the surface effects show perfect tunneling effect, showing zero phase shift. **c**, Matched zero-index metamaterial showing robust scattering-free tunneling against defects.

3.5 Conclusion

In summary, I present the top-down design of bianisotropic acoustic metamaterials. Starting from the top-down design approach that decouples fundamental monopolar and dipolar oscillations, I design a 1-D bianisotropic meta-atom consists of three rooms divided by mass loaded membrane structure made of copper. The proposed meta-atom independently controls all wave parameters near the zero-index point in the water background at 50 kHz operating frequency. In addition, a design approach to a bianisotropic metasurface that manipulates the reflected and transmitted wavefronts has been proposed. In this extended generalized Snell's law, the required structural parameters of metasurface elements are calculated deterministically by inversely retrieving the bianisotropic wave parameters from the target transmission and reflection coefficients. Independent manipulations have been numerically demonstrated in the bianisotropic metasurface made with the proposed 1-D top-down meta-atom platform. Furthermore, a robust 2-D meta-atom design using the space-coiling structure is presented. Because the resonances of space-coiling structure originate from the geometry, the proposed structure can directly applicable to other background media or different systems by scaling to the wavelength. Scattering-free transmission in an array of meta-atom confirmed the zero-index operation of the designed meta-atom structure.

Chapter 4

Virtualized metamaterials

This chapter introduces the concept of virtualization of metamaterials and demonstrates its application in manipulating acoustic wave propagation. By replacing the frequency resonating response of a physical metamaterial structure with a mathematically designed frequency dispersion implemented by digital convolution in the time domain within a microprocessing unit, the impulse response and the form of atomic response of a metamaterial structure is virtualized using a software code for digital representation. In the absence of any physical resonating structure, the digital representation of the virtualized metamaterial permits a highly arbitrary specification of the desired resonating frequency response.

4.1 Introduction to the concept of virtualized metamaterials

Polarizations and scattering process in nature media can be described in the following procedure as depicted in Fig. 4.1: When the external incident waves arrive at the microscopic scatterers, the local fields exerted on them create polarization distribution, and temporal oscillations of polarizations generate subsequent scattering. Total net radiation from the entire particle is the scattered field, and the mixture of these scattered fields and incident fields will be seen as the total fields. The polarization property depends on, and is thus limited by the physical properties such as the composite materials, the scatterer structure, and the frequency of waves in not only conventional materials but also metamaterials with physical structures. On the other hand, in a virtualized metamaterial, the entire polarization process is replaced by the digital signal processing technique: the effective local field is detected by the signal detector, the polarization is calculated by a programmable microprocessor, and the scattering field is generated by an external source that fires the calculated signal output. While the artificial physical structures of metamaterials mimic the working of natural atoms with engineering degrees of freedom, the concept of virtualization generalizes this analogy to a digital representation with tunability based solely on software modification, assigning another level of meaning to “meta.”

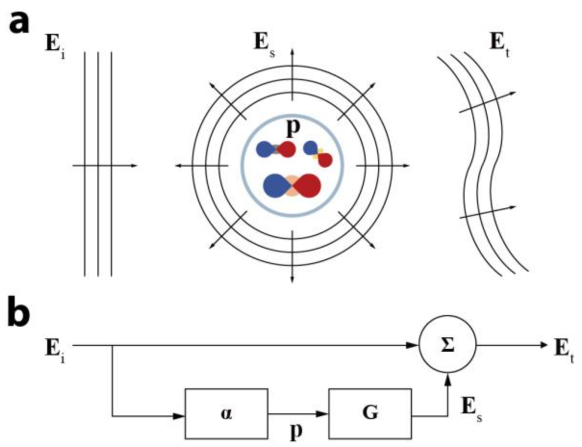

Figure 4.1 | a, Polarization process of the natural scatterer and **b**, its schematic diagram

4.2 Digitally virtualized acoustic polarizations

4.2.1 Virtualization of the signal response of meta-atom

The concept of virtualized metamaterials conceives active metamaterials that utilize digital signal processing technique exactly mimicking this polarization process of natural materials. The virtualized acoustic metamaterial atom comprises a pair of circular microphones situated around two speakers (Fig. 4.2a) and is bonded on a small rectangular holder (lower inset of Fig. 4.2a). This virtualized atom is then placed on the inner side of the top cover of the one-dimensional hollow waveguide to interact but without blocking the sound waves traveling within. For operation, the microphones and speakers are further connected to an external single-board computer (Raspberry Pi 3B+ with analog-to-digital / digital-to-analog conversion module Waveshare ADS1256 / DAC8532). Sound waves arriving at the two microphones are detected, digitally sampled, and then processed in real-time by a software program running on the single-board computer. The resultant digital output signals are then converted back to analog and are feedback to the two speakers to generate the synthesized scattered waves. This combination of microphones, speakers, and software defines the atom's generic scattering response.

Figure 4.2b shows a detailed representation of the software program. I construct a general linear operation from the signals at the two microphones M_1 and M_2 ($M_j(t)$) to the signals at the two speakers S_1 and S_2 ($S_i(t)$) as

$$S_i(t) = -\partial_t^2 (\tilde{Y}_{ij}(t - \delta t) * M_j(t)), \tag{4.1}$$

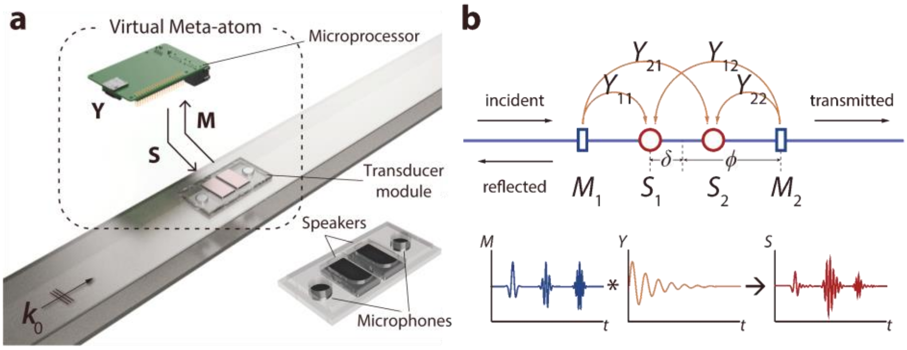

Figure 4.2 | Schematics of the virtualized metamaterial. **a**, Virtualized metamaterial consisting of a structural atom of two circular microphones and two speakers (the two rectangular patches), connected to a small single-board computer for signal processing at a digital level. The virtualized metamaterial is embedded on the inner side of the top cover of a one-dimensional acoustic waveguide, not blocking the incident wave in a passive mode. **b**, Schematic representation of the virtualized metamaterial atom: signals detected at the two microphones (M_1 and M_2) are convoluted with a 2 × 2 matrix (**Y**), resulting in two signals to fire at the two speakers (S_1 and S_2) as secondary radiation from the atom. **Y** is also called the impulse response of the atom. The phase distance between the two speakers is 2δ (actual distance: 2 × 8.5 mm), and the phase distance between the two microphones is 2ϕ (actual distance: 2 × 2.6 cm) for present implementation.

where * denotes convolution operator, and δt represents an extra design time delay in the convolution operation. The whole operation comprises a matrix convolution and a differentiation in time to offset the result of convolution (kernel $\tilde{Y}$ to be designed later) as a driving voltage with zero averaged value for convenient handling within the program. A second time-derivative appears on this voltage since the speaker is actually driven by the voltage in a time-differential way. Finally, a time rate change of the voltage generates sound radiation by the speaker. In the frequency domain, the operation is summarized as

$$S_i(\omega) = Y_{ij}(\omega)M_j(\omega), \tag{4.2}$$

where $Y_{ij}(\omega) = \omega^2\tilde{Y}_{ij}(\omega)\, e^{i\omega\delta t}$. Each orange arrow in the diagram connects a microphone to a speaker and is labeled as one of the matrix elements Y_{ij} of the above operation (hereafter, "convolution"). The main horizontal line (in blue) represents the waveguide direction, in which an incident wave (*e.g.*, from the left) travels and interacts with the atom. The secondary sources at S_1 and S_2 radiate symmetrically both forward and backward. These secondary radiations are added to the incident waves, finally becoming the reflected and transmitted waves within the waveguide. Having specified $Y_{ij}(\omega)$, it is possible to solve the overall response of the whole atom (Fig. 4.2b), yielding transmission/reflection coefficients and the polarizability matrix α_{ij} (or equivalently the scattering matrix s_{ij}) in terms of Y_{ij}. As the polarizability matrix in one-dimensional acoustics is generally 2 × 2, I chose to use two microphones and two speakers to detect and generate both monopolar and dipolar incoming and outgoing waves. Note that all digital computations when performing the convolution can apply only to a finite length of digital signal samples from M_1 and M_2 before the current digital signal sample and must finish within one sampling period (133 μs) of the analog-to-digital conversion module. I also note that while Refs. [66-69] have set up the way to use electronic circuits to replace a physical structure, the further virtualization of the impulse response matrix in our case allows arbitrary specification of the atomic response (amplitude, center frequency, bandwidth, gain/loss, monopolar/dipolar type) and the frequency dispersion through program code without the need to set up different physical structures or different external circuits.

In modeling the constitutive parameters (such as permittivity/permeability in electromagnetism and mass density/ inverse bulk modulus in acoustics) for both natural materials and metamaterials, a Lorentzian frequency dispersion is probably the most representative spectral lines-shape. This acts like an "alphabet," both for analytical modeling and as a numerical measure to decompose an arbitrary frequency spectrum to the sum of Lorentzian components of different spectral parameters. Here, I sought to instruct our virtualized metamaterial to mimic a Lorentzian response as our first example of a virtualized metamaterial. For simplicity, I focus on the monopolar response only, corresponding to an acoustic metamaterial with resonating bulk modulus; the relationship of the effective medium to atomic polarizability will be described later. A monopolar response of the virtualized atom is fulfilled by setting $\tilde{Y}_{11} = \tilde{Y}_{12} = \tilde{Y}_{21} = \tilde{Y}_{22} = \tilde{Y}/2$ in the software. I consider the convolution kernel $\tilde{Y}(t)$ to have the following form:

$$\tilde{Y}(t) = a\,\omega_0^{-2}\sin(\omega_0 t + \theta)\,e^{-\gamma t} \text{ (for } t > 0\text{) or 0 (for } t \leq 0\text{).} \tag{4.3}$$

This involves several model parameters, where ω_0 is resonating frequency, γ is resonating bandwidth, and a is resonance strength. In the formula, these have units of radial frequency, and their values are specified in units of frequency by a factor of $1/2\pi$ for brevity. As an additional parameter to control the shape of frequency dispersion, I also defined θ as the "convolution phase." The software then connects the microphone signals to the speaker signals as in Eq. (4.2), generating the monopolar polarizability of the atom as

$$\alpha_{00} = \frac{c_0}{i\omega} s_{00}(\omega) = \frac{c_0}{i\omega}\frac{2\cos\varphi\cos\delta Y(\omega)}{1-2e^{i\varphi}\cos\delta Y(\omega)} \cong \frac{2c_0}{i\omega} Y(\omega)$$

$$\text{with } Y(\omega) = \frac{\omega^2}{\omega_0^{\ 2}}\frac{a}{2}\left(\frac{e^{i\theta}}{\omega_0+\omega+i\gamma}+\frac{e^{-i\theta}}{\omega_0-\omega-i\gamma}\right)e^{i\omega\delta t} \tag{4.4}$$

where c_0 is the speed of sound in air, and i is the unit imaginary number. All the other polarizability coefficients (α_{11}, α_{01}, and α_{10}) should be zero in this case. For a conventional metamaterial atom, we would expect the monopolar polarizability α_{00}, or the inverse of bulk modulus to have a positive imaginary part for a passive atom. Where $\theta = 0°$ and the convolution delay δt is set to have $\arg(e^{i\omega\delta t}) \approx \pi/2$ at resonating frequency ω_0, the resultant α_{00} mimics the Lorentzian frequency dispersion of a passive acoustic metamaterial in the frequency regime around ω_0. As an example, choosing ω_0 at 1 kHz, γ at 15 Hz and a resonating strength a at 7.85 Hz to implement a passive metamaterial ($\theta = 0°$), $\tilde{Y}(t)$ in Eq. (4.3) is then programmed as the convolution kernel in the virtualized metamaterial atom. To calculate the α or the s matrix, I measured the transmission and reflection coefficients experimentally in both forward and backward directions within the waveguide. The blue curve in Fig. 4.3a represents the frequency trajectory from 750 to 1250 Hz of the experimentally extracted monopolar scattering coefficient s_{ee}. It traces what is roughly a circle, starting near the origin from small frequencies, in a counter-clockwise direction. It falls into the passive regime (indicated by the blue region), with the dashed circle passing through the origin with the center at –0.5. The complex transmission and reflection coefficients (t and r) are simply related to s_{ee} by $t - 1 = r = s_{ee}/2$. In this case, the resonance causes a dip in the transmission spectrum (blue curve in Fig. 4.3b). The Lorentzian shape of both its real and imaginary parts of the monopolar polarizability α_{00} is shown in Fig. 4.3c (blue curves and symbols). The symbols representing the experimental results agree well with the theoretical Lorentzian shape (lines). This constitutes a conventional metamaterial that our virtualized metamaterial approach can mimic.

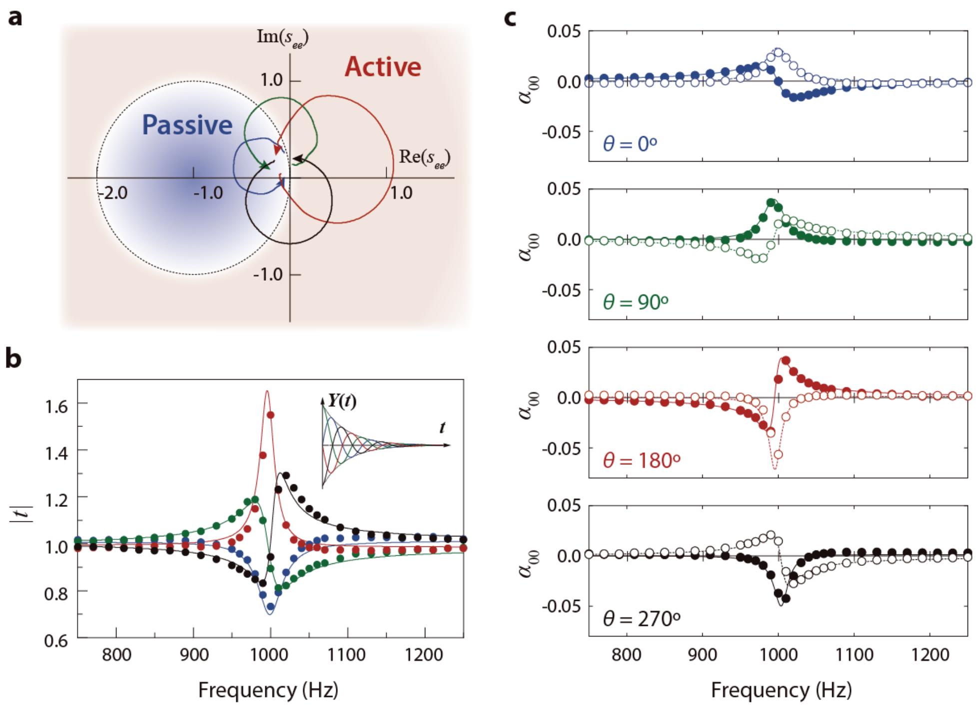

Figure 4.3 | Mimicking Lorentzian frequency dispersion and active acoustic medium with a resonating monopolar response. **a**, Frequency trajectories of the experimental monopolar scattering coefficient s_{ee} on the complex plane for four configurations with convolution phase $\theta = 0°$ (blue), 90° (green), 180° (red), and 270° (black). The red/blue shaded area denotes the active/passive region. Arrows indicate the direction from small to large frequencies. **b**, Transmission amplitude spectrum for the four configurations. The convolution kernel $\tilde{Y}(t)$ for the four different cases of convolution phases are shown in the inset. **c**, The real part (solid symbols) and the imaginary part (empty symbols) of the complex monopolar polarizability α_{00}. Solid and dashed lines denote the corresponding theoretical Lorentzian line shapes for both the real and imaginary parts, respectively.

Although Eq. (4.3) is only a specific class of frequency dispersions, we can now change it by adopting other values of the convolution phase θ to obtain a distinctly different virtual metamaterial. Without needing to design a new physical structure as in the conventional approach to designing metamaterials, the software takes on the role of a physical structure. When θ is changed to 180°, $\tilde{Y}(\omega)$ simply flips signs. It produces an "anti-Lorentzian" shape of α_{00} (red curves and symbols in Fig. 4.3c). The imaginary peak then becomes negative, indicating a simulated material gain. More intuitively, in Fig. 4.3b, the transmission amplitude shows up as a peak beyond a value of one, with the additional power in the transmitted wave drawn directly from the external digital circuits. Figure 4.3a also shows the trajectory of s_{ee} on the complex plane for the virtualized metamaterials at different convolution phases (*e.g.*, θ = 90° and 270°); again, the trajectory is circular. In a geometric picture on the complex plane, the convolution phase θ actually rotates such circles about the origin by the same angle in a clockwise direction. This rotation on the complex plane moves part of the circular trajectory out of the passive zone, making the virtual atom unavoidably active. The virtualized metamaterial now takes on the original role of the swapped real and imaginary parts of the Lorentzian distribution. The real part of α_{00} shows up as a peak while the imaginary part shows up as an oscillation, respectively, shown as green and black in Fig. 4.3c. For conventional metamaterials, a Fano resonance is usually introduced to provide an asymmetric line-shape [95]. Here, we can create an asymmetric line-shape (see $\theta = 90°$ and $270°$ in the $|t|$ spectrum) by tuning the convolution phase value.

The virtualized representation of the metamaterial in Eq. (4.3) provides a straightforward implementation of an active medium. One interesting point is that the anti-Lorentzian shape (effectively the same as a Lorentzian shape but with a negative resonating strength a) has to stand as an approximation in the frequency regime around the resonating frequency. If valid for the whole frequency axis, the poles of the complex function $Y(\omega)$ will occur entirely in the upper half complex plane, denying causal implementation of the convolution kernel. Our approach guarantees causality because it implements the virtual atom by convolution in the time domain. The approximation of the anti-Lorentzian shape around the resonating frequency is linked to the condition $\arg(e^{i\omega\delta t}) \approx \pi/2$, which is only approximately satisfied.

4.2.2 On-demand tuning of dispersion

The virtualized approach to constructing metamaterial allows us to freely reconfigure the frequency dispersion on-demand in a very flexible way. Conventionally, a physical metamaterial design provides both resonating strength and bandwidth at the same time. In principle, these two physical properties (or model parameters) can be reconfigured by two geometric parameters of the metamaterial. However, decoupled control of the two physical properties by two geometric parameters is highly non-trivial[31]. While varying a single geometric parameter often results in a simultaneous change in both physical properties, our approach means that resonating strength and bandwidth are simply two input parameters that can be specified independently, as the convolution kernel ($\tilde{Y}(t)$ in Eq. (4.3)) is defined simply as a mathematical function in the software code for digital representation. Figure 4.5 (a) shows the virtualized metamaterial as specified schematically in Fig. 4.3. The resonating strength a is varied from 3.93, 7.85 to 11.78 Hz while the resonating bandwidth is fixed at γ = 15 Hz. The magnitude and spectral profile of both the real part (solid lines and filled symbols) and the imaginary part (dashed lines and empty symbols) of the monopolar polarizability increase and scale with a. Similarly, I reduced the resonating bandwidth γ from 30 to 15 and 7.5 Hz to obtain sharper resonance with a being kept at a constant value of 7.85 Hz. The results are shown in Fig. 4.4b; in both cases, the experimentally obtained frequency dispersions of monopolar polarizability α_{00} (plotted in symbols) agree well with the theoretical model derived from $Y(t)$, where the solid and dashed lines represent its real and imaginary parts, respectively. In fact, as the magnitude of $Y(t)$ decays in time through $\exp(-\gamma t)$, the smallest γ we can achieve is limited by the total convolution time (T_c) implemented in the software code. A smaller γ requires a larger T_c if the magnitude of $Y(t)$ is to decay to a negligible value before truncation. For example, a requested 10dB decay in $Y(t)$ before truncation was chosen for accurate implementation of the target $Y(t)$ with γ as small as 3.4 Hz. In these cases, the resonating frequency was kept at 1 kHz. Finally, we fixed γ = 15 Hz and a = 7.85 Hz and then varied the resonating frequency ω_0 from 0.8 to 1.2 kHz in steps of 100 Hz. Clear resonances were observed around the designated resonating frequencies, with a tunable range of resonating frequencies approaching almost 40% of the central frequency in the tunable range ($\Delta\omega/\omega$), which is limited only by the speed of the electronics. Faster electronics can further increase the digital sampling frequency to achieve a higher frequency bound, while the convolution (accomplished digitally within one sampling period) can involve more samples. I also note that the tunability offered by our approach can become more flexible and generic. As $Y(t)$ is a mathematical function freely encoded in the software, we can render the frequency dispersion to have a more general shape, for example, to capture multi-resonating frequencies, each with different strengths, bandwidths, and with either gain or loss.

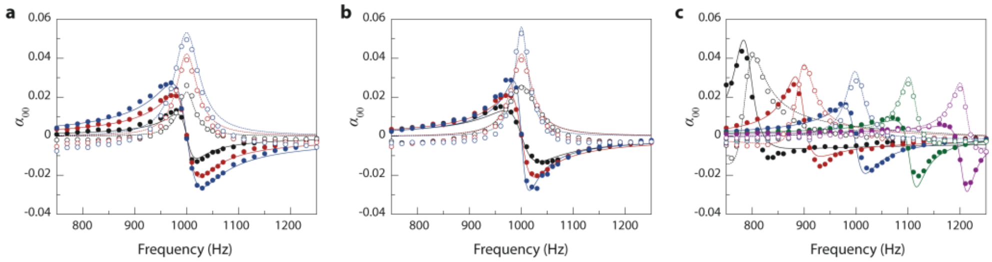

Figure 4.4 | Decoupled tuning of resonance amplitude, bandwidth, and center frequency for the virtualized metamaterial. **a**, Three cases of resonating strength a = 3.93 (black), 7.85 (red) and 11.78 Hz (blue) with constant resonating bandwidth γ = 15 Hz and resonating frequency ω_0 = 1 kHz. The real/imaginary part of monopolar polarizability α_{00} is plotted in solid/empty symbols for the experimental results. **b**, Three cases of resonating bandwidth γ = 30 (black), 15 (red) and 7.5 Hz (blue) with constant resonating strength a = 7.85 Hz. **c**, Resonating frequency ω_0 varies from 800 to 1200 Hz in steps of 100 Hz with γ = 15 Hz and a = 7.85 Hz. Here an extra phase shift is inevitable because of the inherent time delay in electronic devices as the resonance frequency increases. The corresponding theoretical models are plotted in solid/dashed lines for the real/imaginary part in all panels.

4.2.3 Independent control of monopolar and dipolar scattering

Connecting monopolar incidence to monopolar scattered waves corresponds to an acoustic metamaterial with a resonating bulk modulus. Our virtualized approach can also be used to construct metamaterials with a more general response than monopolar scattering. As our atom has sufficient degrees of freedom when generating both monopolar and dipolar secondary radiations, the same virtualized metamaterial technique can be used to generate a dipolar scattering response, corresponding to an effective resonating density. In this case, I set $\tilde{Y}_{11} = -\tilde{Y}_{12} = -\tilde{Y}_{21} = \tilde{Y}_{22} = \tilde{Y}/2$ and the dipolar scattering coefficient is then given by

$$\alpha_{11} = \frac{c_0}{i\omega} s_{11}(\omega) = \frac{2c_0}{i\omega} \frac{2\sin\varphi \sin\delta Y(\omega)}{1 + 2ie^{i\varphi} \sin\delta Y(\omega)} \cong \frac{4c_0}{i\omega} \sin\varphi \sin\delta Y(\omega). \qquad (4.5)$$

$\tilde{Y}(t)$ and $Y(\omega)$ are still defined in Eq. (4.3) and in Eq. (4.4) (with subscript 1 added to a and γ to indicate the dipolar nature of the model parameters). To demonstrate, I set a resonating frequency ω_0 = 1.2 kHz, resonating strength a_1 = 14.25 Hz and linewidth γ_1 = 8 Hz; I also set the convolution phase θ = 0°, corresponding to the passive case. The resultant real and imaginary parts of α_{11} are shown in Fig. 4.5a as the black solid and dashed curves with resonating behavior. This corresponds to a resonating mass density (in an effective medium of the virtualized metamaterial) with a positive resonating peak in its imaginary part. On the other hand, if we change the convolution phase θ to 180° (with the same parameters for ω_0, a_1 and γ_1), the resonating atoms are gain-dominating around the resonating frequency, showing a negative peak in the imaginary part of α_{11} in Fig. 4.5b. In the same Fig. 4.5a,b, the corresponding values of monopolar response α_{00} (shown in red) have much smaller amplitudes than the instructed dipolar response.

By exploiting the virtualized metamaterial's degrees of freedom, the monopolar resonance and dipolar resonance can be generated at the same time. More importantly, all of the resonating model parameters can be designed as highly arbitrary. For the implementation, I set $\tilde{Y}_{11} = \tilde{Y}_{22} = (\tilde{Y}_0 + \tilde{Y}_1)/2$ and $\tilde{Y}_{12} = \tilde{Y}_{21} = (\tilde{Y}_0 - \tilde{Y}_1)/2$ where $\tilde{Y}_0$ and $\tilde{Y}_1$ are implemented by Eq. (4.3) with resonating strength a_0 and a_1 and resonating linewidth γ_0 and γ_1, with the resonating frequency commonly set at $\omega_0 = 1.2$ kHz. As shown in Fig. 4.5c, both s_{00} and s_{11} are now resonating. Model values are detailed in the caption to Fig. 4.5. The virtualized atom can also be immediately transferred to the gain regime by changing θ from 0° to 180°, as shown in Fig. 4.5d; the resonating peak of the imaginary part for both α_{00} and α_{11} goes negative as a dominating gain around resonance. I have been using polarizability to represent the atomic property. On the other hand, our 1-D metamaterial can be equivalently represented as an effective medium of thickness d (actual thickness of our atom = 6.5 cm), the relationship between the effective bulk modulus B and the effective mass density ρ can be related to the monopolar and dipolar polarizabilities as

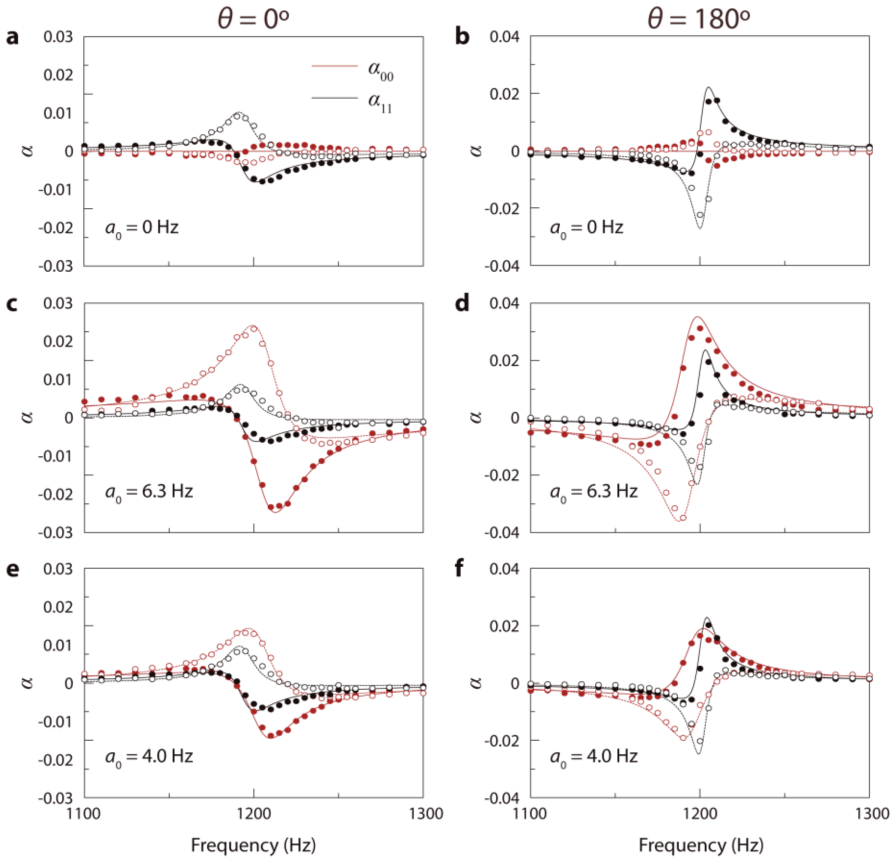

Figure 4.5 | Decoupled control on the monopolar and dipolar scattering coefficients. **a**,**b**, Virtualized metamaterial with only dipolar response where the model parameters are set as γ_1 = 8 Hz, a_1 = 14.2 Hz, resonating frequency ω_0 = 1.2 kHz and convolution phase θ = 0° (**a**) and 180° (**b**). **c,d,** Monopolar response is further added to configurations in (**a,b**) with model parameters γ_0 = 15 Hz, a_0 = 6.3 Hz with the same ω_0. **e**,**f**, Monopolar response is changed to a_0 = 4 Hz while other model parameters are kept the same. For all results, the left/right panel shows the scattering coefficients for convolution phase θ = 0° (**a,c,e**) and 180° (**b,d,f**).

$$\chi_0 = \frac{B^{-1}}{B_0^{-1}} - 1 \cong \frac{\alpha_{00}}{d}$$
$$\chi_1 = \frac{\rho}{\rho_0} - 1 \cong \frac{\alpha_{11}}{d} \tag{4.6}$$

where B_0 and ρ_0 are the bulk modulus and the mass density of the air, respectively, while χ_0 and χ_1 refer to monopolar and dipolar. The ability to control both monopolar and dipolar polarizabilities is essential in order to control the transmission and reflection amplitudes simultaneously through $t - 1 = (S_{ee} + S_{oo})/2$ and $r = (S_{ee} - S_{oo})/2$. I note that the near-field coupling (as there is no physical structure) if we periodically place identical atoms along the propagation direction, can be neglected. The effective medium parameters are still valid when we scale up the number of atoms.

Unlike conventional metamaterials that require the design of a special kind of atom, the virtual implementation of metamaterials allows density and modulus to be independently tuned without affecting each other and without modifying any physical structures or external circuits. Figure 4e,f show the corresponding results for the model parameters in Fig. 4.5c,d ($\theta = 0°$ and 180°) but with the resonating strength a_0 divided by a factor of 1.6. The results show that dipolar resonance is almost unaffected while monopolar resonance (*e.g.*, the peak of Im(α_{00})) is divided by roughly the same factor. Our results confirm the advantages of the virtualization approach in designing tailor-made configurations, addressing some of the inherent limitations of conventional metamaterial approaches by allowing the model parameters to be tuned to any desired value. This also contrasts with common approaches in which the resonating strength and bandwidth of active metamaterials are unlikely to be independently configurable because they depend on actual mechanisms to achieve gain. Moreover, while dipolar resonance is much sharper than monopolar resonance in conventional metamaterials, the virtualized approach can make the two resonances are similar in shape and bandwidth (see Fig. 4.5e). This enables impedance matching (to achieve small reflectance) in a wide frequency regime. In short, the present virtualized approach offers great advantages for modifying metamaterial resonance.

4.2.4 Transient response of the virtual metamaterial

The response of a resonating metamaterial generally depends on the Q-factor, or equivalently the resonating linewidth, of the resonance. The response time can be measured experimentally by using a step function (with the carrier frequency, e.g., 1 kHz) as input to drive the incident wave. As an example, we shine such an incident wave on the metamaterial with different resonating linewidth γ = 7.5, 15, and 30 Hz. As shown in Fig. 4.6, the response time, defined as the time to get half of the steady-state amplitude, is found as 29, 14, and 7 ms, which is roughly proportional to $1/\gamma$.

On the other hand, we can also fire a transient signal with a varying amplitude as a wave packet for the incident wave, instead of getting the monopolar response at separate frequencies by firing continuous waves at different frequencies. Here, the responses from 750 to 1250 Hz are measured in one single transient experiment by inverse Fourier transforming the measured signal at various microphones. Figure 4.7a shows the input pulse (quadratic spline) with a duration of 5.0 ms and 2.5 ms. The carrier frequency of the pulse is set as 1 kHz. Such an incident transient pulse is fired to the metamaterial, with the configuration in Fig. 4.3 with convolution phase θ = 0° and resonating linewidth γ = 15 Hz. Figure 4.7b,c shows the corresponding experimental spectrum (solid/empty symbols for real/imaginary part) obtained for the monopolar polarizability. As we can see, the results follow the theoretical spectrum (in lines) very well, even up to a pulse width as short as 5.0 ms, which is much shorter than the response time of 14 ms, indicating the metamaterial can work for transient excitations. When the pulse width is further reduced, we see higher noise as the total power of the incident wave is now spread across a wider range of frequencies.

On the other hand, the response time (due to electronics and digital sampling) can be probed by firing a pulse to our metamaterial but with a non-resonating response (small resonating strength). Figure 4.8 shows a typical incident pulse (in black line) and the measured scattering from the metamaterial (red dashed line). It is found that the response time is around 500 ms, which includes all the physical and electronic delays between the microphones and speakers with feedback.

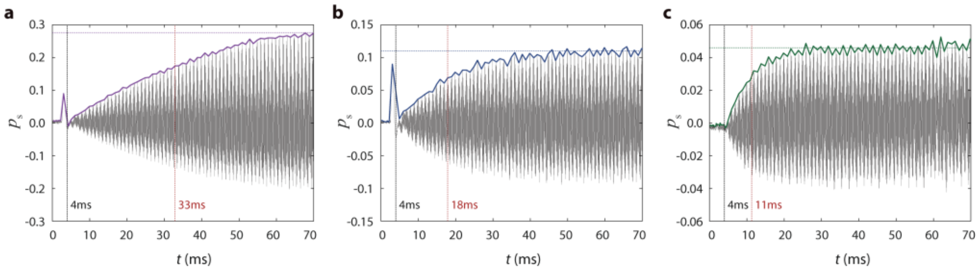

Figure 4.6 | Transient response for step-type input at a fixed frequency. Typical response time to approach steady-state with amplitude response agreeing to target spectrum for (**a**) resonating linewidth γ = 7.5 Hz, (**b**) 15 Hz, and (**c**) 30 Hz for same resonating frequency 1 kHz and the same incident step function with carrier frequency 1 kHz in experiments. Smaller γ has a shorter response time. The time constant for each bandwidth is given by 29 ms, 14 ms, and 7 ms.

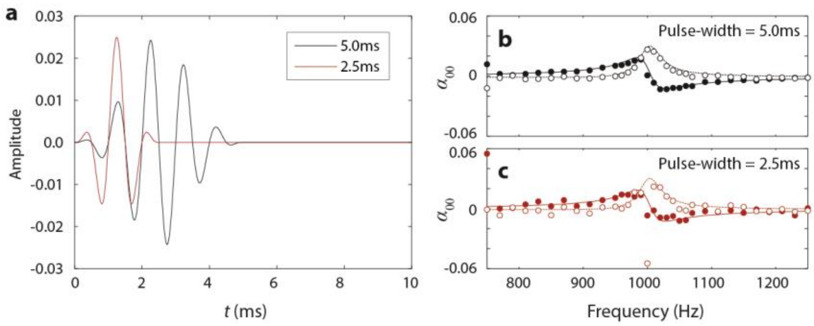

Figure 4.7 | **a**, Transient response for finite pulses. The input (quadratic spline) pulses with a finite duration of 5.0 ms or 2.5 ms, and carrier frequency 1 kHz in driving the incident waves. **b**,**c**, The monopolar polarizability measured from the metamaterial in Figure 4.3 with convolution phase θ = 0° and resonating linewidth γ = 15 Hz.

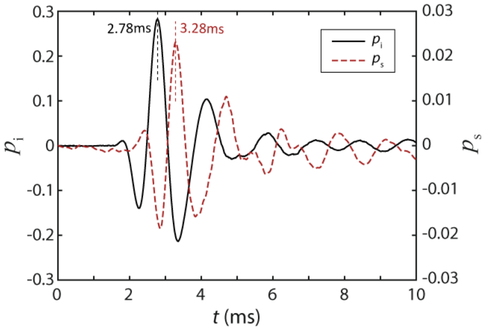

Figure 4.8 | Response time for a non-resonating metamaterial. Incident (p_i) and scattering (p_s) waves of a non-resonating metamaterial in probing the ultimate response time, due to all physical and digital electronic delay.

4.3 Experimental setup

The experimental set-up is schematically shown in Fig. 4.2a. A meta-atom consists of two speakers and two microphones with electric peripherals, including a microprocessor, analog-to-digital/digital-to-analog converter, and amplifying modules. For the digital convolution, the microprocessor is programmed to operate at a sampling frequency of 7.5 kHz and using 400 sampling data to accomplish all calculation process within one cycle. Speakers and microphones which are connected to the microprocessor and communicate through the serial peripheral interface, are assembled in an acrylic frame (width = 3.0 cm, length = 6.5 cm). This transducer module is mounted on top of a one-dimensional rectangular acoustic waveguide (width = 6.0 cm, height = 2.0 cm). For the measurement, I used the 4-points measurement method with the National Instrument DAQ device and Labview system. The scattering parameters spectra can also be obtained by doing a transient stimulus using a wave packet of finite duration and a carrier frequency.

4.4 Conclusion

In conclusion, I have proposed and provided experimental support for the concept of virtualized metamaterials, removing the physical restrictions of traditional metamaterials. Using a convolution kernel function and digitally driven wave sources to synthesize the scattered wave directly, it was possible to freely access different frequency dispersion curves on demand, achieving decoupled control on different wave parameters and constitutive parameters. The software-controlled transition between Lorentzian, anti-Lorentzian, and asymmetric dispersion curves were experimentally confirmed within a single platform while independently addressing amplitude, center frequency, bandwidth, and convolution phase for all dispersion curves across a broad frequency range. The frequency dispersion, equivalently the impulse response function, can be programmed to other shapes to achieve optimal bandwidth for material constitutive parameters [66], material gain, zero-index, etc. In fact, the frequency dispersion of the material parameters can be further modulated in time slowly (comparing to the sampling period), we can then apply such dynamic modulation on individual atoms to construct time-varying metamaterials [96]. For example, a modulation phase lag between different atoms can be used to generate an Aharonov–Bohm phase and non-reciprocal transmission [97], which can now be readily achieved in acoustics. Furthermore, we can also use an ensemble of these virtualized atoms to realize Floquet topological phases with a temporally periodic Hamiltonian [98,99].

For our platform, gain and loss can also be matched exactly and varied in the time domain due to the flexible tunability, allowing us to investigate non-Hermitian systems [100,101] with exceptional points that can now be scanned through dynamically and without any physics structures. It should also be straightforward to inverse-derive the mathematical kernel for a virtualized metamaterial on demand for targeted applications and wave parameters. This approach is not limited to the acoustic platform, as the implementation of the convolution kernel function can also be envisaged in FPGA, for the faster convolution required in ultrasonic or microwave applications.

Chapter 5

Extreme Acoustic Properties

beyond the Passivity and Reciprocity Bounds

This chapter discusses the feasibility of the virtualized metamaterials to provide extreme acoustic wave properties that hardly achievable. I assess the ultimate bound of Willis coupling and the conditions for nonreciprocity and implement ideas using virtualized metamaterials. By achieving selective excitation of the inverse bulk modulus, and the mass density, I demonstrate the ultimate Willis bound and extreme nonreciprocity within the same platform as a universal building block for future Willis applications. I further realize Willis atom operation with broadband and flat dispersion, in both the purely reciprocal and purely nonreciprocal regimes, from analytically constructed dispersion curve via the inverse design method.

5.1 Introduction to the limit of bianisotropic media

Despite the great successes achieved thus far, the full potential of bianisotropic acoustic metamaterials has not been achieved. First, The maximum bound of Willis coupling and nonreciprocal operation, which are inherent to the passivity of the metamaterial structure, currently hinders the full exploitation of the advantages offered by Willis metamaterials in future applications. Although the breaking of the passive Willis bound or the tuning of nonreciprocity have been envisaged with the introduction of active metamaterials, the question of how to achieve selective excitation and flexible control of all four constitutive parameters to enable extreme bianisotropy and fully controllable nonreciprocity has yet to be answered.

5.2 Extreme acoustic properties

5.2.1 Bianisotropy beyond the passivity bound

To realize independent manipulation of all polarizability, I define a scattering matrix **S** having parity symmetry in the one-dimensional system as depicted in Fig. 5.1, for incident (a) and scattered (b) waves propagating in the forward (+) and backward (–) directions, which are decomposed into components of even (e) and odd (o) parity: $a_e = (a_+ + a_-)/2$, $a_o = (a_+ - a_-)/2$, $b_e = (b_+ + b_-)/2$, and $b_o = (b_+ - b_-)/2$. The couplings between the incident fields and scattered fields are then written as $(b_e\ b_o)^T = \mathbf{S}\ (a_e\ a_o)^T$, with the scattering matrix **S** being defined as

$$\begin{pmatrix} s_{ee} & s_{eo} \\ s_{oe} & s_{oo} \end{pmatrix} = \frac{1}{2}\begin{pmatrix} t_+ + t_- + r_+ + r_- - 2 & t_+ - t_- + r_+ - r_- \\ t_+ - t_- - r_+ + r_- & t_+ + t_- - r_+ - r_- - 2 \end{pmatrix}, \tag{5.1}$$

where r and t are the reflection and transmission coefficients, respectively. Then the relation between the scattering matrix **S** and the normalized polarizability $\boldsymbol{\alpha}$ becomes:

$$\begin{pmatrix} \alpha_{pp} & \alpha_{pv} \\ \alpha_{vp} & \alpha_{vv} \end{pmatrix} = \frac{1}{ik_0}\begin{pmatrix} s_{ee} & s_{eo} \\ s_{oe} & s_{oo} \end{pmatrix}, \tag{5.2}$$

where k_0 is the free space wavenumber. In this representation, the diagonal terms relating even-incident to even-scattering components (s_{ee}) and odd-incident to odd-scattering components (s_{oo}) correspond to the inverse bulk modulus and mass density, respectively, while the coupling of the off-diagonal components even to odd components (s_{oe}) and odd to even components (s_{eo}) are the acoustic bianisotropy or Willis coupling parameters. Although our consideration of Willis coupling does not assume passivity and reciprocity in general, it is worth mentioning that for a conventional passive and reciprocal metamaterial, reciprocity is equivalently represented by $t_+ = t_-$ or $s_{eo} = -s_{oe}$, and the maximum Willis coupling corresponds to $|s_{eo}|$ (or $|s_{oe}|$) = 1, which is difficult to achieve while keeping the other components intact.

To realize all these polarization responses with selective excitation and precise balancing between the cross-coupling terms, inverse bulk modulus, and mass density, we employ a platform of a virtualized meta-atom, which can directly mold the above parameters with the designer convolution function connecting the detectors and sources. As depicted in Fig. 5.2, the microprocessor returns output values to two speakers (S_i) from the detected signals of two microphones (M_j) by means of the programmed convolution kernels ($\tilde{Y}_{ij}$). I.e., the output voltages of the sources are calculated in the time domain as follows:

$$S_i(t) = -\partial_t^2(\tilde{Y}_{ij}(t) * M_j(t)), \tag{5.3}$$

where * is the convolution operator, and the subscripts i, j = 1 or 2 are the labels of the speakers and microphones. In Eq. (5.3), one derivative is given by the software for a zero averaged offset value, and the other derivative appears in speakers when generating a pressure field in a time differential way. In the frequency domain, the entire operation is summarized as $S_i(\omega) = Y_{ij}(\omega)M_j(\omega)$ where $Y_{ij}(\omega) = \omega^2\tilde{Y}_{ij}(\omega)$. To achieve a connection between the speaker output S_i and the microphone-detected signal M_j, similar to the polarization process in Eq. (5.1), we decompose the convolution kernel Y_{ij} by introducing a basis of convolution matrices:

$$\mathbf{e}_{ee} = \frac{1}{2}\begin{pmatrix} 1 & 1 \\ 1 & 1 \end{pmatrix},\ \mathbf{e}_{eo} = \frac{1}{2}\begin{pmatrix} -1 & 1 \\ -1 & 1 \end{pmatrix},\ \mathbf{e}_{oe} = \frac{1}{2}\begin{pmatrix} -1 & -1 \\ 1 & 1 \end{pmatrix},\ \mathbf{e}_{oo} = \frac{1}{2}\begin{pmatrix} 1 & -1 \\ -1 & 1 \end{pmatrix}, \tag{5.4}$$

which satisfy $\mathbf{Y} = Y_{ee}\,\mathbf{e}_{ee} + Y_{eo}\,\mathbf{e}_{eo} + Y_{oe}\,\mathbf{e}_{oe} + Y_{oo}\,\mathbf{e}_{oo}$. Eq. (5.3) can then be rewritten in terms of the symmetric (even) and antisymmetric (odd) components of the speakers and microphones as follows:

$$\begin{pmatrix} S_1 + S_2 \\ S_2 - S_1 \end{pmatrix} = \begin{pmatrix} Y_{ee} & Y_{eo} \\ Y_{oe} & Y_{oo} \end{pmatrix}\begin{pmatrix} M_1 + M_2 \\ M_2 - M_1 \end{pmatrix}. \tag{5.5}$$

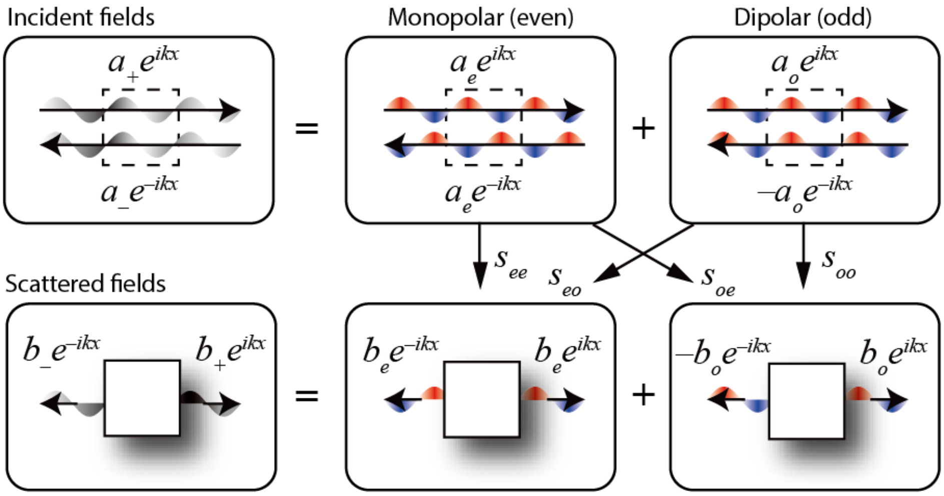

Figure 5.1 | The definition of the scattering matrix **S** in a one-dimensional system. The incident and resultant scattered fields propagating in the forward and backward directions are decomposed into even and odd components. The even-to-even and odd-to-odd scattering parameters correspond to the inverse bulk modulus and density, respectively, while the even-to-odd and odd-to-even scattering parameters are the Willis parameters.

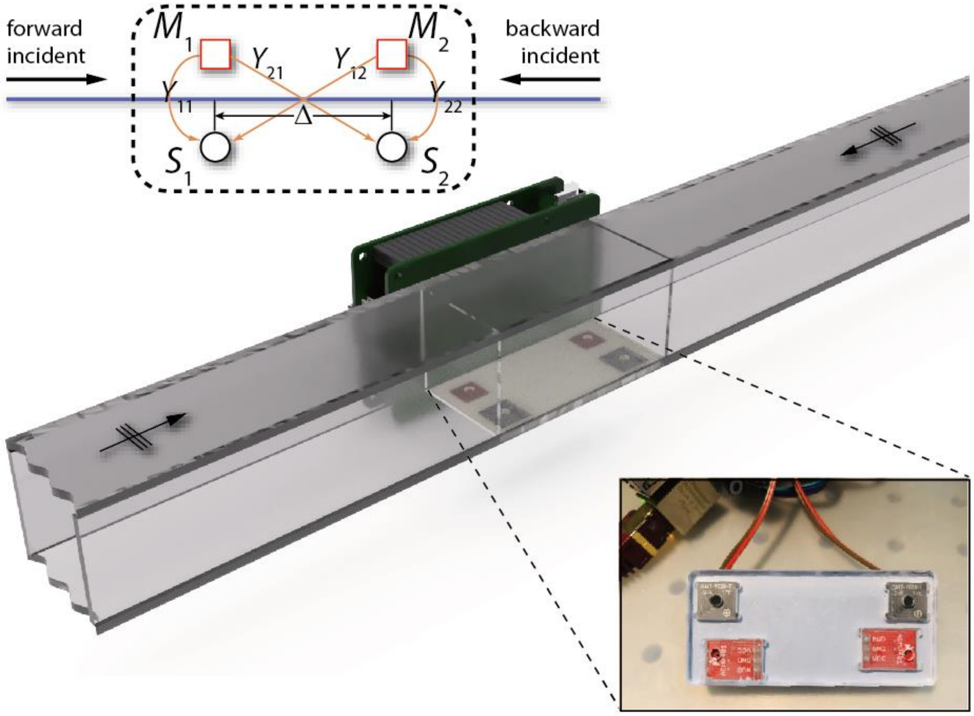

Figure 5.2 | Bianisotropic virtualized metamaterial. A virtualized metamaterial consisting of two microphones and two speakers connected to a microprocessor embedded in the cover of an acoustic waveguide. The bottom-right inset shows a photograph of a transducer module of a virtualized meta-atom. The top inset shows an analytical representation of the virtualized metamaterial atom: two microphones (M_j) are convolved with a 2 × 2 matrix (Y_{ij}) returning signals to fire at the two speakers (S_i) as secondary radiation. The distances between the two speakers and microphones are equally set to $\Delta = 50$ mm. The scattering property of the meta-atom is tested by incident waves coming from the forward and backward directions to identify all four scattering parameters (r_+, t_+, r_-, and t_-).

It is important to note that in this representation, in terms of a basis of convolution matrices, each basis matrix $\mathbf{e}_{kl}$ exclusively addresses one of the four polarizability parameters, including the two Willis parameters. In our atom configuration shown in Fig. 5.2, in the case of selective excitation (i.e., $\mathbf{Y} = Y_0\,\mathbf{e}_{ij}$), the polarizability parameters can then be written as follows:

$$
\begin{aligned}
\alpha_{pp} &= \frac{4}{ik_0}\frac{\cos\left(k_0\Delta/2\right)^2 Y_0}{1-\left(1+e^{ik_0\Delta}\right)Y_0}, \\
\alpha_{pv} &= 2k_0^{-1}\sin\left(k_0\Delta\right)Y_0, \\
\alpha_{vp} &= -2k_0^{-1}\sin\left(k_0\Delta\right)Y_0, \\
\alpha_{vv} &= \frac{4}{ik_0}\frac{\sin\left(k_0\Delta/2\right)^2 Y_0}{1-\left(1-e^{ik_0\Delta}\right)Y_0}.
\end{aligned}
\tag{5.6}
$$

where Δ is the distance between the two speakers (and microphones). Therefore, decoupled control or balancing among all acoustic wave parameters can be realized with analytically constructed kernels Y_{ij} of the desired design. It is emphasized that the relationship derived in Eq. (5.6) is analogous to the effective medium theory expression that relates the constitutive parameters to the scattering parameters of composite scatterers.

5.2.2 Extreme nonreciprocity

Figure 5.3 shows an experimental demonstration of the selective excitation of each polarizability parameter in the virtual Willis metamaterial. We set the program to have one of the basis convolution matrices $\mathbf{e}_{ee}$, $\mathbf{e}_{eo}$, $\mathbf{e}_{oe}$, and $\mathbf{e}_{oo}$, given in Eq. (5.4) with the Lorentzian-form coefficient $\tilde{Y}_0(\omega)$. For time-domain microprocessor signal processing, $\tilde{Y}_0(\omega)$ can then be expressed or implemented as the following impulse response function:

$$\tilde{y}_0(t) = \frac{a}{\omega_0^{\,2}} \sin(\omega_0 t + \theta) e^{-\gamma t} u(t), \tag{5.7}$$

where $u(t)$ is the Heaviside step function, $a = 15$ is the total scaling factor, $\omega_0 = 1.0$ kHz is the resonance frequency, $\theta = -\pi/2$ is the phase, and $\gamma = 15$ Hz is the resonance bandwidth. Figure 5.3a,b show the Lorentzian polarizations experimentally realized with even-to-even $\mathbf{e}_{ee}$ and odd-to-odd $\mathbf{e}_{oo}$ excitations, which are responsible for inverse bulk modulus and mass density, respectively, and Fig. 5.3c,d show the implementation of bianisotropy achieved with odd-to-even $\mathbf{e}_{eo}$ and even-to-odd $\mathbf{e}_{oe}$ convolutions. Each polarization component is exclusively excited, with the other components suppressed, in excellent agreement with the analytical results in Eq. (5.6). Since this approach enables simultaneous independent control of the four wave parameters, by balancing the even-to-odd and odd-to-even couplings, we can also easily realize the *purely* reciprocal and nonreciprocal Willis parameters $\kappa = i(\alpha_{pv} - \alpha_{vp})/2$ and χ

= $(\alpha_{pv} + \alpha_{vp})/2$ from the symmetric convolution kernels $\mathbf{Y} = Y_0(\mathbf{e}_{eo} + \mathbf{e}_{oe})$ for the reciprocal case (Fig. 5.3e) and the antisymmetric $\mathbf{Y} = Y_0(\mathbf{e}_{eo} - \mathbf{e}_{oe})$ in the nonreciprocal case (Fig. 5.3f). Our results are not subject to the strict restriction imposed by the geometry of the scatterers in physical metamaterials, in contrast with previous approaches, in which the resonance strengths and bandwidths of individual polarization components are unlikely to be independently configurable. It is further noted that because the virtualized Willis metamaterial can also handle complex polarizabilities, it is possible to achieve controllable gain and loss of the system as well as complex bianisotropy, enabling phenomena such as imaginary reciprocal and nonreciprocal coefficients, which are impossible with conventional bianisotropic media.

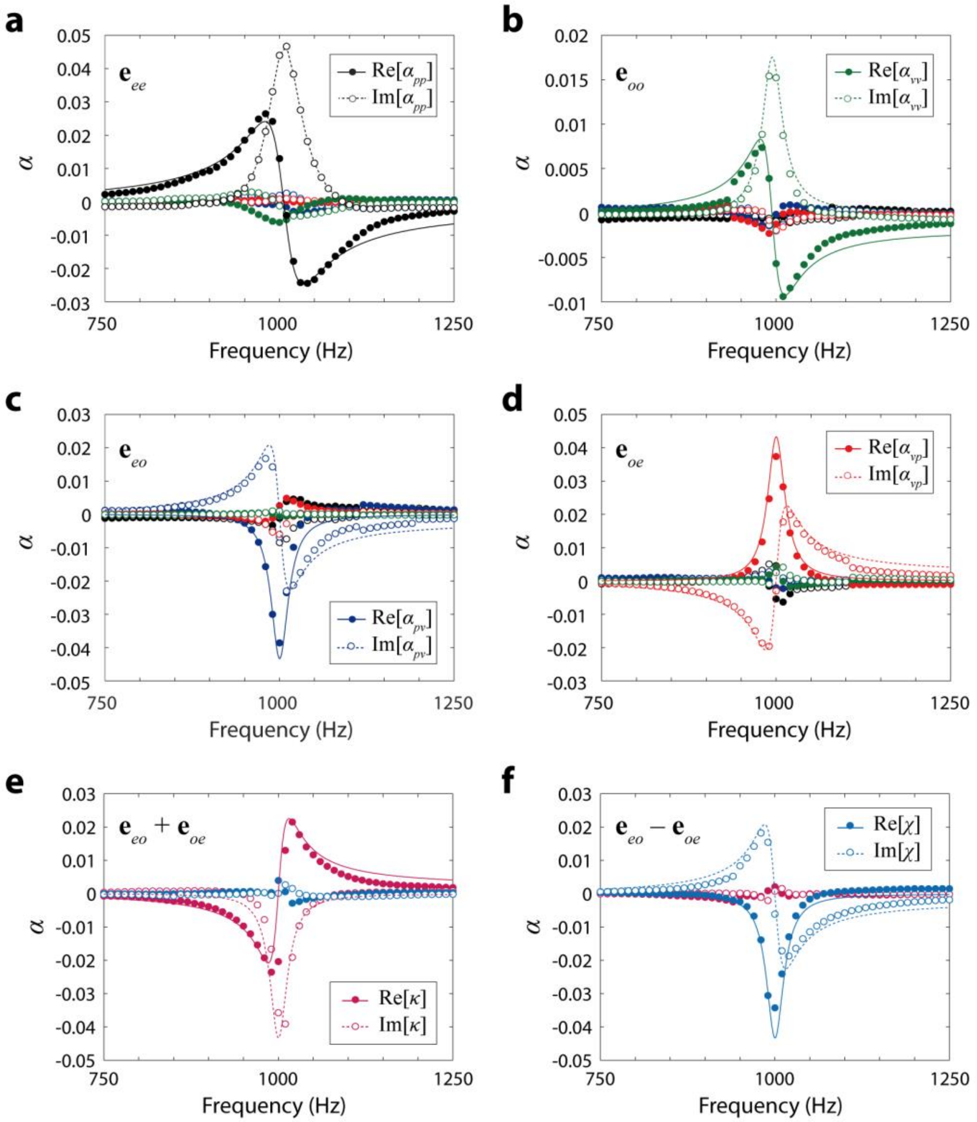

Figure 5.3 | Decoupled excitation of polarization components. a-d, Virtualized Willis metamaterial for the four basis convolution matrices $\mathbf{e}_{ee}$ (**a**), $\mathbf{e}_{oo}$ (**b**), $\mathbf{e}_{eo}$ (**c**), and $\mathbf{e}_{oe}$ (**d**) with the same Lorentzian convolution kernel Y_0, where the model parameters are set to a = 15, $\theta = -\pi/2$, γ = 15 Hz, and ω_0 = 1.0 kHz. The polarizabilities α_{pp}, α_{vv}, α_{pv}, and α_{vp} are depicted in black, green, blue and red, respectively, with solid/empty symbols representing the real/imaginary parts of the experimental results. The corresponding

theoretical models are plotted with solid/dashed lines for the real/imaginary parts. **e**,**f**, Purely reciprocal and purely nonreciprocal Willis couplings $\kappa = i(\alpha_{pv} - \alpha_{vp})/2$ and $\chi = (\alpha_{pv} + \alpha_{vp})/2$, realized with a balanced $\mathbf{e}_{oe}$ and $\mathbf{e}_{eo}$. The purely reciprocal Willis coupling satisfying $\alpha_{vp} = -\alpha_{pv}$ is demonstrated by their summation, i.e., $\mathbf{Y} = Y_0(\mathbf{e}_{eo} + \mathbf{e}_{oe})$ (**e**), and the purely nonreciprocal term satisfying $\alpha_{vp} = \alpha_{pv}$ is demonstrated by subtracting the two basis convolution matrices, $\mathbf{Y} = Y_0(\mathbf{e}_{eo} - \mathbf{e}_{oe})$ (**f**).

The ability to excite Willis coupling is known to be limited by the passivity condition, as discussed earlier. Following the derivation in Ref. [86] for two- and three-dimensional systems, for the one-dimensional passive system treated here, the maximum bianisotropy bound is dictated by the following two inequalities :

$$\begin{aligned} &\left|s_{oe}\right|^2 + \left|1+s_{ee}\right|^2 \le 1, \\ &\left|s_{eo}\right|^2 + \left|1+s_{oo}\right|^2 \le 1. \end{aligned}, \tag{5.8}$$

or, equivalently in terms of polarizability,

$$\begin{aligned} &\left|k_0\alpha_{vp}\right|^2 + \left|1+ik_0\alpha_{pp}\right|^2 \le 1, \\ &\left|k_0\alpha_{pv}\right|^2 + \left|1+ik_0\alpha_{vv}\right|^2 \le 1. \end{aligned}, \tag{5.9}$$

Thus, the maximum bound of the Willis coupling is given by $|\alpha_{vp}|(|\alpha_{pv}|)\le k_0^{-1}$, where the equality is satisfied when α_{pp} (α_{vv}) = ik_0^{-1}. If the systems are strictly reciprocal, e.g., in the case of a physically designed structure with curled channels, we can set $t_+ = t_-$, and then, the inequality is reduced to $|r_+ - r_-| \le 2$ as an upper bound on the Willis coupling term for a reciprocal scatterer. In this passive case, one needs to design a system with $t_+ = t_- = 0$ and $r_+ = -r_- = e^{i\varphi}$, where φ is the arbitrary real number needed to approach the equality in the inequality. However, with our implementation using a virtualized metamaterial, we need not be restricted by the reciprocity and maximum bound of the Willis coupling. Because the secondary radiation source in our virtualized metamaterial draws power from external digital circuits, it becomes straightforward to overcome the maximum bound of the Willis coupling.

Figure 5.4 shows the magnitudes of the Willis couplings $|\alpha_{pv}|$ (Fig. 5.4a) and $|\alpha_{vp}|$ (Fig. 5.4b) for Lorentzian convolution kernels with two different scaling factors (a = 15 and 30) at different resonance frequencies (f_0 = 900 Hz, 1000 Hz, and 1100 Hz) and with a fixed bandwidth (γ = 15 Hz). All cases show a central peak at the resonance frequency where the Willis coupling is maximized, in agreement with the analytical models in Eq. (5.6). In contrast to the maximum bianisotropy of a passive metamaterial (black dashed line), which is dictated by $|\alpha_{vp}|$ (or $|\alpha_{pv}|$) = k_0^{-1}, the newly established maximum bianisotropy for the virtualized Willis metamaterial (magenta dotted line) is now modified to $|\alpha_{vp}|$ (or $|\alpha_{pv}|$) = $2k_0^{-1}|\sin(k_0\Delta)Y_0|$ with $|Y_0| \approx a/2\gamma$ at the resonance frequency, revealing the set of parameters for controlling the Willis coupling strength. It is worth mentioning that the presence of $k_0\Delta$ in $\sin(k_0\Delta)$ reveals the required metamaterial geometry of the scatterer (or source) layout, while the amplitude a, bandwidth γ, and center frequency ω_0 reveal the significance of the scatterer characteristics. At the values Δ = 50 mm and γ = 15 Hz used in the experiment, Fig. 5.4 shows theoretical (lines) and experimentally realized (symbols) Willis parameters with the scaling factor of a = 15 and a = 30 respectively, each for below and above the passivity bound (black-dashed lines). In addition to the control parameter a, which represents the power drawn by the active devices, it is further noted that the layout of the scatterers, represented by Δ, can also be used to control the strength of the polarizability. In our implementation, a small $\Delta \sim \lambda/7$ was used, in the regime of metamaterials without further optimization. With the introduction of a resonance directly into the Willis coupling term, the system will draw the necessary power from the external source, i.e., become active, and the conventional Willis bound can intuitively be surpassed.

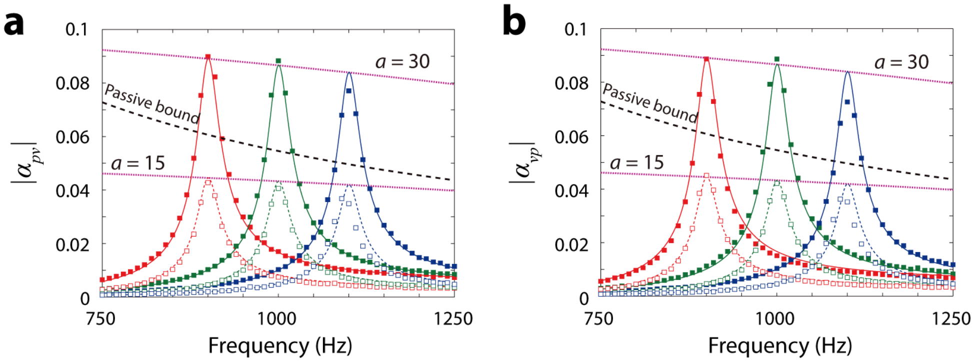

Figure 5.4 | Willis coupling beyond the passivity bound. Willis coupling beyond the passivity bound achieved by controlling the scaling factors. **a**, The magnitude of α_{pv} for the odd-to-even convolution kernel $\mathbf{e}_{eo}$. The Lorentzian responses at three center frequencies, f_0 = 900 Hz (red), 1000 Hz (green), and 1100 Hz (blue), are demonstrated with two different scaling factors, a = 15 (empty symbols) and 30 (filled symbols). The analytical results for each scaling factor are also plotted as solid and dashed lines, and the magenta dotted lines denote the theoretical values of the Lorentzian peaks at the resonance frequencies. The black dashed line represents the passivity limit of Willis coupling, i.e., $|\alpha_{pv}| = k_0^{-1}$. **b**, Same as **a** except that $|\alpha_{vp}|$ for the even-to-odd convolution kernel $\mathbf{e}_{oe}$ is demonstrated.

5.2.3 Broadband-, flat-frequency dispersion

Recalling that there is no reason for the frequency response of Y to be limited to a Lorentzian response in our implementation, here, we address a metamaterial realization with an arbitrary target response function $F_0(\omega)$ based on the notion of inverse design. To realize $\alpha_{pv}(\omega)$ (or $\alpha_{vp}(\omega)$) = $F_0(\omega)$, we utilize the relation in Eq. (5.6) and obtain the convolution function $Y_{eo}(\omega) = F_0(\omega)k_0 \sin(k_0\Delta)^{-1}/2$ (or $Y_{oe}(\omega) = -F_0(\omega)k_0 \sin(k_0\Delta)^{-1}/2$) for the target frequency response F_0. By applying inverse Fourier transformation to $Y_{eo}(\omega)$ (or $Y_{oe}(\omega)$), we can numerically obtain the required time-domain convolution function $y(t)$. As metamaterials restrict $k_0\Delta$ to be small, the resultant time-domain function of this inverse design process will be similar to the inverse Fourier transform of the original target frequency response $F_0(\omega)$. For example, we consider an intriguing target frequency spectrum with a flat broadband response between ω_1 and ω_2, specifically,

$$\begin{aligned} F_0(\omega) = e^{i\theta}&\left[\frac{1}{2}\left(\operatorname{sgn}(\omega+\omega_1)-\operatorname{sgn}(\omega+\omega_2)\right)+\frac{i}{\pi}\log\left|\frac{\omega+\omega_1}{\omega+\omega_2}\right|\right] \\ -e^{-i\theta}&\left[\frac{1}{2}\left(\operatorname{sgn}(\omega-\omega_1)-\operatorname{sgn}(\omega-\omega_2)\right)+\frac{i}{\pi}\log\left|\frac{\omega-\omega_1}{\omega-\omega_2}\right|\right], \end{aligned} \tag{5.10}$$

which satisfies the Kramers-Kronig (KK) relation, along with its inverse Fourier transform,

$$f_0(t) = \frac{2}{\pi}\frac{a}{t}\left[\sin(\omega_1 t+\theta)-\sin(\omega_2 t+\theta)\right]u(t)\,. \tag{5.11}$$

When ω_2 is set to be much larger than ω_1, the above function $F_0(\omega)$ with θ = 0 ($\theta = \pi/2$) provides a flat real (imaginary) spectrum over a broad frequency range while suppressing the imaginary (real) part, while peaks appear in the vicinity of ω_1 and ω_2. This $F_0(\omega)$ could thus be used to design broadband Willis metamaterials offering purely real or purely imaginary polarizability.

To demonstrate the purely reciprocal and nonreciprocal Willis couplings, also with broadband characteristics, we then program the convolution kernel to be $\mathbf{Y} = Y_0(\mathbf{e}_{eo} + \mathbf{e}_{oe})$ for the reciprocal case and $\mathbf{Y} = Y_0(\mathbf{e}_{eo} - \mathbf{e}_{oe})$ for the nonreciprocal case, as used in the narrowband demonstrations shown in Fig. 5.3e,f. Figure 5.5 shows the experimental realization of the purely reciprocal Willis parameter $\kappa = i(\alpha_{pv} - \alpha_{vp})/2$ and the purely nonreciprocal parameter $\chi = (\alpha_{pv} + \alpha_{vp})/2$, achieving a flat broadband spectrum over (ω_1, ω_2) = (800 Hz, 1200 Hz) for $\theta = 0$ (Fig. 5.5b,c) and $\theta = \pi/2$ (Fig. 5.5a,d), with $a = 0.225$. It is important to note that while Fig. 5.5a,b each correspond to conventional Willis couplings for omega media and moving media, which have real components of κ and χ, respectively, the Willis couplings shown in Fig. 5.5c,d newly achieve imaginary κ and χ values, providing an additional degree of freedom in terms of energy, i.e., gain and loss in the Willis coupling. We note that while even more general frequency responses can be constructed beyond the Lorentzian resonance and flat dispersion demonstrated here, it is necessary to keep some reservations due to the causality restriction. For example, the required time-domain convolution function from the inverse

Fourier transform of the target frequency response could contain anti-causal components, i.e., $y(t) \neq 0$ for $t < 0$. Nonetheless, we are open to the possibility of mitigating at least the condition of $y(t < 0) \neq 0$ through some modification of the virtual metamaterial configuration, such as placing the microphones before the speakers. In essence, our virtualization scheme provides a one-step implementation, through the digitization of the impulse response as a software entity, to obtain any physically allowed broadband spectrum. The same approach can be readily applied in other applications requiring a broadband response. For example, it can also be applied to design causality-optimal sound absorption media, with the advantage that once the causality-optimal spectrum has been formulated, there is no need to formulate a strategy further to obtain the corresponding metamaterial structures. In other words, by adopting the virtualization approach, one does not need to be concerned with passivity and reciprocity, which are the usual starting points for formulating performance bounds, but rather can relax the necessary considerations to causality only. In our case, causality is considered automatically through the KK relation.

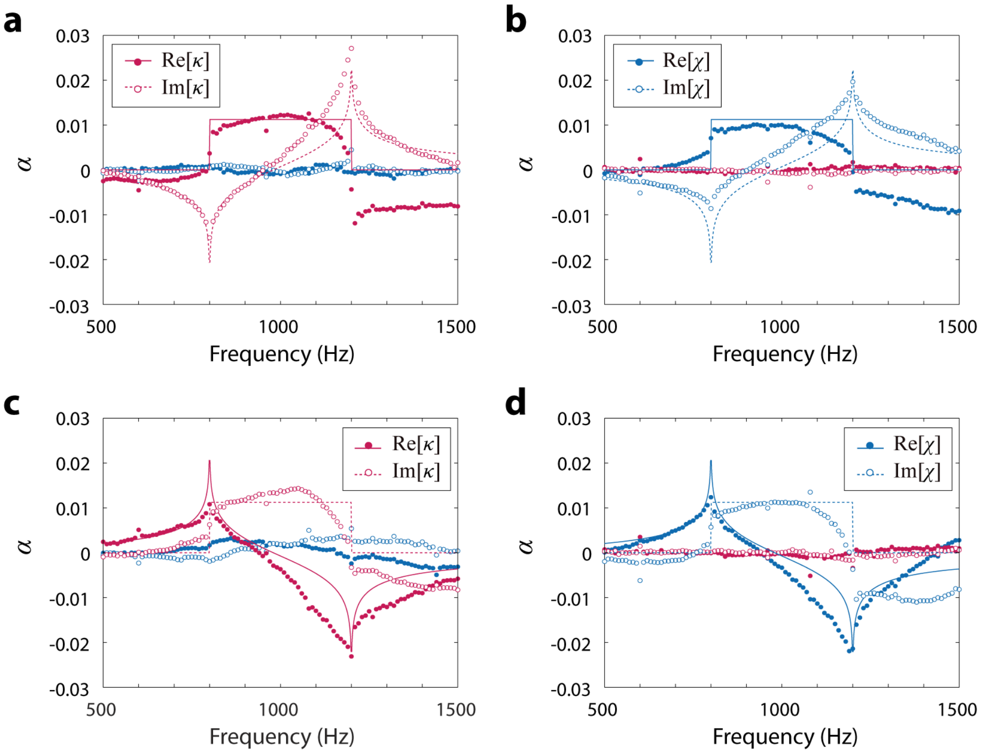

Figure 5.5 | Broadband frequency dispersion control of Willis couplings. Experimental demonstration of Willis coupling parameters inversely designed from a frequency dispersion response with broadband flat real values, while imaginary values are restricted in the vicinity of the band edges. By balancing α_{pv} and α_{vp}, **a**,**c** broadband purely reciprocal Willis coupling parameters $\kappa = i(\alpha_{pv} - \alpha_{vp})/2$ and (b,d) broadband purely nonreciprocal Willis coupling parameters $\chi = (\alpha_{pv} + \alpha_{vp})/2$ are achieved. **a** and **b** correspond to conventional omega media and moving media with real κ and χ, while **c** and **d** show imaginary reciprocal and nonreciprocal Willis couplings, which are not naturally achievable.

5.3 Experimental setup

The bianisotropic virtualized meta-atom consists of two MEMS microphones (INMP401) and speakers (SMT-1028-t-2-r) laterally located on each edge of the acrylic frame, which are connected to an external single-board computer (Raspberry Pi 4B+) with amplifiers and analog-to-digital/digital-to-analog converters (see Fig. 5.2). For digital processing, the input signals sampled by the microphones are digitally processed by the microprocessor and then fed to the speakers in real-time with a sampling frequency of f_s = 7.5 kHz and a number of samples equal to N = 400. The convolution is calculated as $S_i^V[n] = \sum_j \sum_{k=0}^{N} Y_{ij}[k]\left(M_j[n-k] - M_j[n-k-1]\right)$, where the index $n = t/T_s$ is the discrete-time with sampling period $T_s = f_s^{-1}$. The speakers and microphones, which communicate with the microprocessor through the SPI (Serial Peripheral Interface), are mounted in an acrylic frame (width = 3.0 cm, length = 6.5 cm). This transducer module is, in turn, mounted on the acoustic waveguide (width = 3.0 cm, height = 3.0 cm).

5.4 Conclusion

In this chapter, I demonstrate active bianisotropic metamaterials offering Willis coupling beyond the passivity limit. The conditions for maximum Willis coupling and reciprocity in the passivity regime are revisited, and then, the new bound of the Willis parameter and the reciprocity with the introduction of an active metamaterial are analyzed. By employing a virtualized metamaterial platform that enables the flexible design of scattering properties by means of software convolution functions, Lorentzian resonances of all of the polarizability parameters are demonstrated, with exclusive access to each polarizability, including the Willis parameters, inverse bulk modulus, and mass density, independently. Using the fully independent excitation of each parameter as well as precise balancing between them, the operations of purely reciprocal and nonreciprocal Willis couplings are realized. We also demonstrate the breaking of the Willis bound in the passivity limit for the first time while isolating the control parameters involved with the newly established Willis bound in the active regime, such as the amplitude, bandwidth, and frequency of the active resonator that feeds in external power for the scattered fields. Finally, we achieve the inverse design of target Willis responses with identical, flat-amplitude Willis coupling strengths over a broad frequency range, for the reciprocal and nonreciprocal cases as well as the newly revealed case of nonconserved bianisotropy.

Chapter 6

Conclusion

In this Dissertation, the top-down design of acoustic metamaterials has been demonstrated for the decoupled and reconfigurable control of extraordinary wave properties. From the idea that decouples fundamental oscillations of wave parameters, a deterministic approach to provide target wave properties in a single platform is investigated. With the physical metamaterial structure, cross-shaped acoustic metamaterials using a mass on a membrane and space-coiling resonator are proposed, which enable independent manipulation of bulk modulus, mass density, and bianisotropy. These metamaterial structures confirm deterministic operations of bianisotropic metasurface, manipulating both reflection and transmission wavefronts and scattering-free propagation in matched-zero index metamaterials. Extending the top-down approach of physical metamaterials, I propose the concept of virtualized metamaterials that mimics polarization process of natural media, offering reconfigurable and decoupled manipulation of wave properties. I fabricate one-dimensional acoustic virtualized metamaterials using the microprocessor with electric peripherals and the real-time digital convolution and show independent control of all entity of wave parameters based on the decoupling of fundamental wave parameters. Virtualized metamaterials could realize extraordinary physical properties such as non-Hermiticity, bianisotropy beyond the passivity bound, and extremely high nonreciprocity. It is confirmed that any dispersion satisfying causality would be realized from the software-controlled transition between Lorentzian, anti-Lorentzian, and broadband-, flat dispersion.

Demonstrating full control and top-down tailoring of all wave parameters within the same platform, this work would achieve the full potential of acoustic metamaterials and their diverse applications beyond conventional bound of passivity and nonreciprocity.

Appendix A

Supplements for Chapter 4

A.1 Monopolar and dipolar model of the virtualized atom

For a one-dimensional (1-D) system (along x-direction), we express the total pressure and the velocity (in the propagating direction in x) by

$$\begin{aligned} p &= a_0 \cos(kx) + a_1 \sin(kx) + b_0 e^{ik|x|} + b_1 \operatorname{sgn}(x) e^{ik|x|}, \\ \rho c_0 v_x &= a_0 i \sin(kx) + a_1 \cos(kx) + b_0 \operatorname{sgn}(x) e^{ik|x|} + b_1 e^{ik|x|}, \end{aligned} \tag{A.1}$$

where p and v_x are the pressure and velocity fields, respectively, ρ and c_0 are the density and the sound speed in air. The monopolar (dipolar) incident waves are denoted by a_0 (a_1), while the monopolar (dipolar) scattered waves are denoted by b_0 (b_1) in generating symmetric (antisymmetric) waves, see Figure A.1 for the schematic representation. The response of the artificial atom can be denoted by the scattering matrix **S**:

$$\begin{pmatrix} b_0 \\ b_1 \end{pmatrix} = \mathbf{S} \begin{pmatrix} a_0 \\ a_1 \end{pmatrix} = \begin{pmatrix} s_{00} & s_{01} \\ s_{10} & s_{11} \end{pmatrix} \begin{pmatrix} a_0 \\ a_1 \end{pmatrix} \tag{A.2}$$

which can also be written in terms of transmission (t) and reflection (r) coefficients in the forward (subscript f) and backward (subscript b) directions:

$$\mathbf{S} = \frac{1}{2} \begin{pmatrix} t_f + t_b + r_f + r_b - 2 & t_f - t_b + r_f - r_b \\ t_f - t_b - r_f + r_b & t_f + t_b - r_f - r_b - 2 \end{pmatrix} \tag{A.3}$$

The response of the system can be equivalently described by $\mathbf{Y}(\omega)$ matrix for convolution operation (in Fig. 4.2b) or the scattering matrix $\mathbf{S}(\omega)$. They are related to each other by

$$\begin{aligned} \begin{pmatrix} M_1 \\ M_2 \end{pmatrix} &= \mathbf{Y}^{-1} \begin{pmatrix} S_1 \\ S_2 \end{pmatrix} \\ &= \begin{pmatrix} \cos\phi & -i\sin\phi \\ \cos\phi & i\sin\phi \end{pmatrix} \mathbf{S}^{-1} \begin{pmatrix} \cos\delta & \cos\phi \\ i\sin\delta & -i\sin\phi \end{pmatrix} \begin{pmatrix} S_1 \\ S_2 \end{pmatrix} + \mathbf{G} \begin{pmatrix} S_1 \\ S_2 \end{pmatrix} \end{aligned} \tag{A.4}$$

where **G** is the structure factor in describing the propagation from two speakers S_1, S_2 to microphones M_1, M_2 and is defined by

$$\mathbf{G} = e^{i\phi} \begin{pmatrix} e^{-i\delta} & e^{i\delta} \\ e^{i\delta} & e^{-i\delta} \end{pmatrix}, \tag{A.5}$$

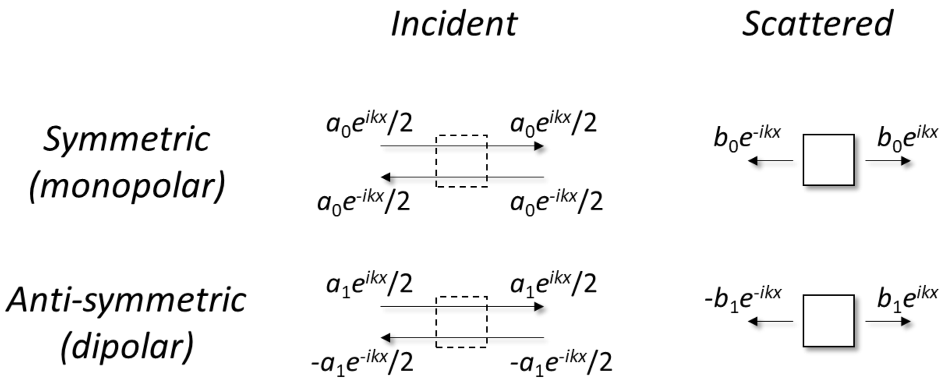

Figure A.1 | The schematic diagram for monopolar and dipolar models of the virtualized atom. The scattering process is defined as a monopolar response when the symmetric input generates the symmetric scattering field (upper). On the contrary, an anti-symmetric input generates an anti-symmetric scattering field (lower) is defined as a dipolar response. Here $a_{0,1}$ and $b_{0,1}$ represent amplitudes of the incident and scattered waves, respectively. The center of the virtualized atom is set at the origin.

where 2ϕ is the phase distance between two microphones and 2δ is the phase distance between two speakers (see Fig. 4.2b). **G** modifies the response matrix **Y** since microphones detect incoming waves plus the secondary radiation generated by speakers. Such a "renormalization" from the circuit response to the overall atomic response is common. It also occurs in the effective medium theory for an ensemble of isolated dipoles: the macroscopic and local fields are different so that susceptibility is proportional to polarizability in the dilute limit but goes to the Maxwell-Garnett formula as filling fraction increases due to a similar renormalization.

From the relationship between **S** and **Y**, we can solve **S** from given **Y**. For example, the scattering matrix for the monopolar atom in Figs. 4.3 and 4.4 can be obtained by substituting $Y_{11} = Y_{12} = Y_{21} = Y_{22} = Y/2$ to obtain

$$\mathbf{S}(\omega)=\frac{2Y(\omega)}{\sec\delta-2Y(\omega)e^{i\phi}}\begin{pmatrix}\cos\phi & 0\\ 0 & 0\end{pmatrix} \tag{A.6}$$

Similarly, we can also readily obtain a virtualized metamaterials with dipolar scattering response by redesigning the $[Y]$ matrix as $Y_{11} = -Y_{12} = -Y_{21} = Y_{22} = Y/2$. Then the scattering matrix $[\mathcal{D}](\omega)$ becomes

$$\mathbf{S}(\omega)=\frac{2Y(\omega)}{\csc\delta+2iY(\omega)e^{i\phi}}\begin{pmatrix}0 & 0\\ 0 & \sin\phi\end{pmatrix} \tag{A.7}$$

Theoretically, only the dipolar scattering coefficient S_{11} is nonzero in **S** matrix, but the discrepancy between two speakers of the atom inevitably generates small amounts of monopolar secondary radiation in the experiment. Therefore, the monopolar scattering coefficient S_{00} becomes nonzero, but is very small compared to the dipolar scattering coefficient S_{11}, as shown in Fig. 4.5a,b. In a more conventional way to describe the response of the atom, we can use the polarizability $\boldsymbol{\alpha}$, which is related to the **S** matrix by

$$\boldsymbol{\alpha}(\omega)=\begin{pmatrix}\alpha_{00}(\omega) & \alpha_{00}(\omega)\\ \alpha_{00}(\omega) & \alpha_{00}(\omega)\end{pmatrix}=\frac{c_0}{i\omega}\mathbf{S}(\omega) \tag{A.8}$$

A.2. Power gain of active metamaterials

Figure A.2 plots the power gain $|r|^2 + |t|^2$ for configurations in Fig. 4.3, confirming the outgoing power is larger than the input power.

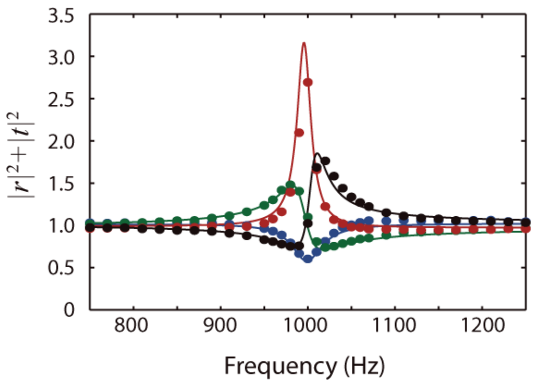

Figure A.2 | Metamaterial power gain. The spectrum for the sum of transmission intensity and reflection intensity for the 4 configurations (in Fig. 2) with convolution phase θ = 0° (blue), 90° (green), 180° (red) and 270° (black), where symbols and lines denote the experimental and theoretical results respectively. Here $|r|^2 + |t|^2$ is the power gain for one-side incidence.

A.3 Effective medium parameters and impedance matching

As shown in Fig. 4.5, the monopolar and dipolar response of the virtualized metamaterial can be controlled independently. Therefore, we can readily realize the decoupled control on the effective medium parameters since the system can be regarded as an effective medium, which breaks through those limitations inherent to the physical structures. The spectrum of the effective medium parameters is determined by Eq. (4.6), as shown in Fig. A.3. For the virtualized metamaterial with dipolar response only (Fig. A.3a,b, the monopolar resonance strength a_0 = 0), the dipolar susceptibility χ_1, which is associated with the effective mass density ρ, is dominated over the monopolar susceptibility χ_0 for both the case of convolution phase θ = 0° and 180°. When the monopolar resonance strength a_0 increases from 0 to 6.3 Hz, the monopolar susceptibility χ_0 emerges (Fig. A.3c,d). The virtualized metamaterial behaves like an ensemble of isolated dipolar and monopolar resonance. Therefore, we can further adjust the dipolar and monopolar resonance independently to realize the impedance matching. Readjust the resonance strength a_0 to 4.0 Hz, only the monopolar susceptibility χ_0 decreases while the dipolar susceptibility χ_1 keeps the same (Fig. A.3e,f). In this case, the inverse of effective bulk modulus B^{-1} and the effective mass density ρ are almost equivalent, which represents the realization of impedance matching ($Z = (\rho/B^{-1})^{1/2} \approx 1$). As a result, we can adjust the reflection and transmission amplitudes and achieve small reflectance in a wide frequency regime as shown in Fig. A.4.

On the other hand, the connection from the single-atom polarizabilities to the bulk property (multiple atoms) can be obtained from Eq. 4.6. In our metamaterial atom in a 1D system, the near field in coupling the neighboring unit cells (along the propagating direction) is not significant. The following simulation shows that the wavefront quickly goes to plane wave within 5 cm, which is comparable to the size of each atom (6.5 cm), and much smaller than the wavelength of acoustic wave (34 cm).

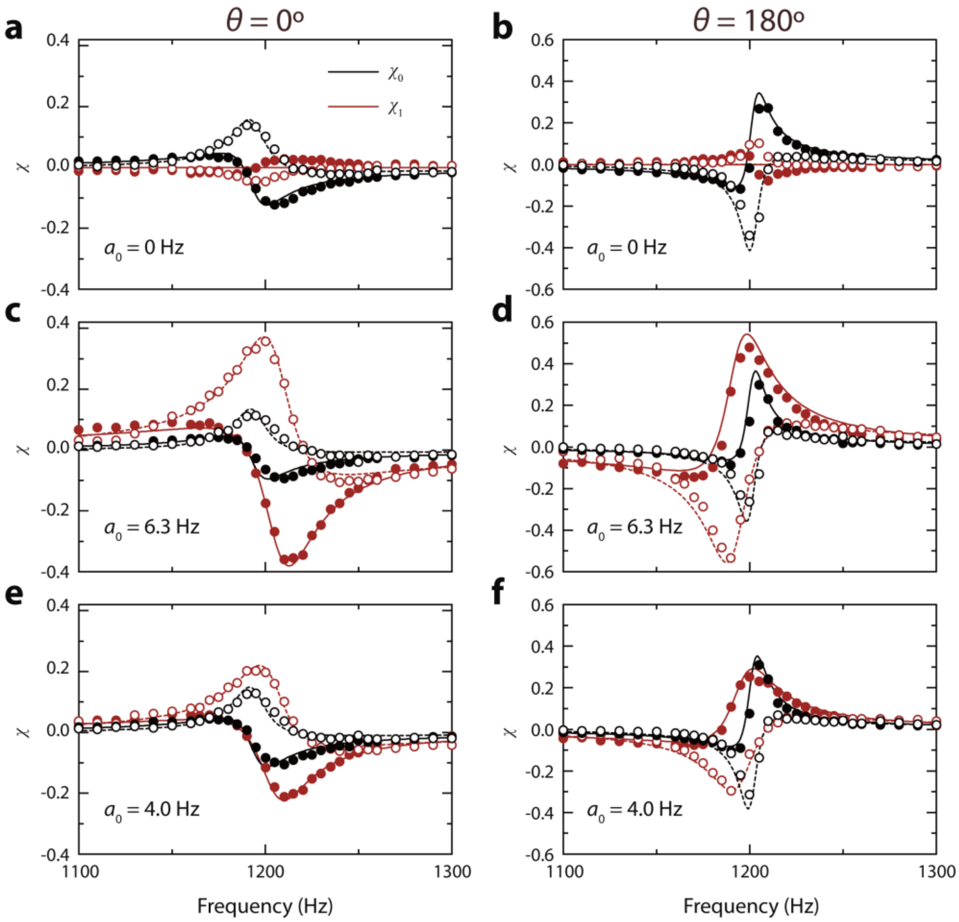

Figure A.3 | The effective medium parameters of the virtualized metamaterial. The monopolar and dipolar susceptibilities χ_0 (red) and χ_1 (black) for the convolution phase of θ = 0° and 180°. (**a**,**b**) When the virtualized metamaterial has a dipolar response only, the dipolar susceptibility χ_1, associated with the effective density ρ, is dominated in this case. (**c**,**d**) The monopolar susceptibility χ_0 which is associated with the effective bulk modulus B of the virtualized metamaterial emerges after adding the monopolar response. (**e**,**f**) The monopolar susceptibility χ_0 decreases while χ_1 keeps the same when we lower the resonance strength a_0. For all results, lines and symbols represent the theoretical and the experimental results, respectively. The left and right panels show the scattering coefficients for the convolution phase of θ = 0° and 180°.

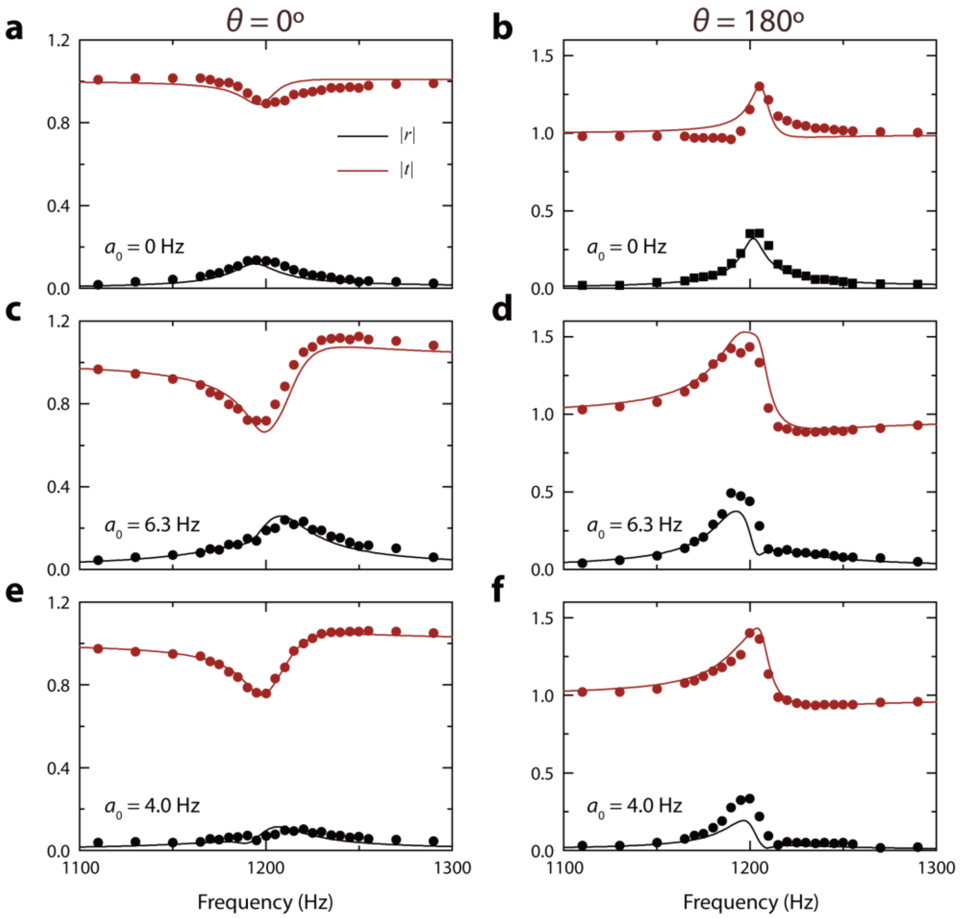

Figure A.4 | The reflection and transmission amplitudes. The reflection amplitude $|r|$ (black) and transmission amplitudes $|t|$ (red) the convolution phase of $\theta = 0°$ and 180°, when the virtualized metamaterial has a dipolar response only (**a**,**b**), the monopolar response is added (**c**,**d**), and the monopolar resonance strength a_0 is decreased to realize the impedance matching (**e**,**f**). For all the cases of convolution phase $\theta = 180°$ (right panel), the virtualized atom is working in the active regime and the peak of the transmission amplitudes beyond the unity

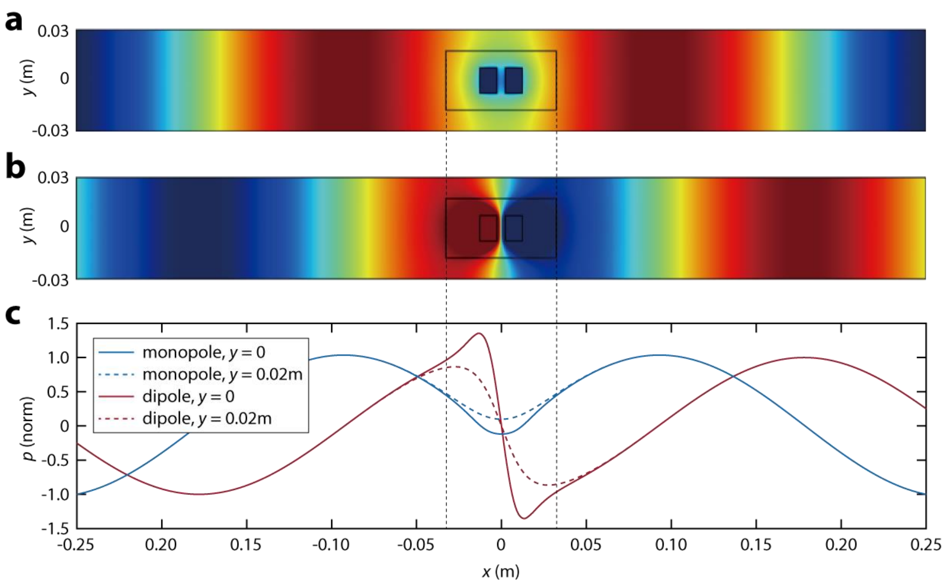

Figure A.5 | The plane wave generation from meta-atom speakers. **a**,**b**, Numerical simulations of meta-atom sources generating (**a**) monopolar (symmetric) and (**b**) dipolar (anti-symmetric) scattering fields. **c**, Pressure field profiles measured at $y = 0$ (solid line) and $y = 0.02$ m (dashed line) for monopolar (blue) and dipolar (red) sources, where the wavefront goes to plane wave within 0.05 m. Speakers modeled by 1×1.5cm flat rectangular structure are 1.7 cm away from each other and mounted in 2×6 cm rectangular waveguide.

This is in the so-called transmission-line metamaterial regime in which the near-field coupling between neighboring unit cells becomes negligible while the coupling between the neighboring unit cells is only through far-field. With this background, the single-atom property also represents the bulk property when atoms are cascaded in the propagating direction. Figure

A.6a shows the more traditional representation of effective medium parameters of the same type of atoms in Fig. 4.3 (with a smaller resonance strength and convolution phase 180°), now in terms of an anti-Lorentzian resonating reciprocal bulk modulus and a unit density (not shown here). Solid lines/symbols are the extracted model/experimental values. Black/blue represents the real/imaginary part. Then, by using these effective single-atom medium properties, we can calculate the expected two-atoms and three-atoms properties, transmission amplitude and phase spectra are shown in Fig. A.6b,c, as solid lines, which also agree to the experimental results shown in symbols, showing the validity in using single atom property in scaling up to the situation of multiple atoms.

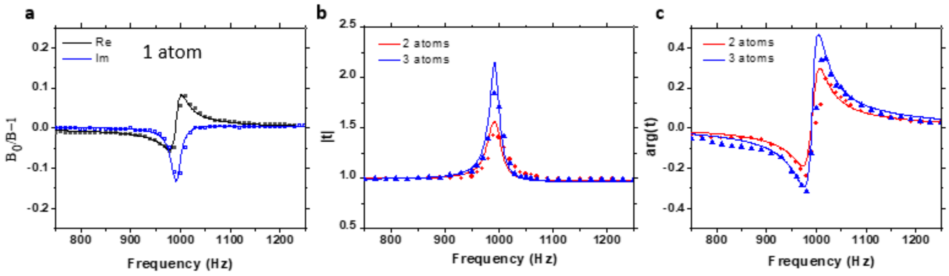

Figure A.6 | Response from multiple atoms. **a**, Effective medium parameters extracted from a single atom with convolution phase $\theta = 180°$. Solid lines (symbols) represent theoretical (experimental) results. The real (imaginary) part is shown in black (blue) color. **b,c**, Transmission from cascading 2 or 3 atoms of the same configuration. Experimental results, (**b**) for two atoms and (**c**) 3 atoms, are shown in symbols, while solid lines represent the theoretical results that are obtained from the previous single-atom property shown in (**a**).

Appendix B

Supplements for Chapter 5

B.1 Derivation of the relationship between the polarizability and the scattering matrix

It is well known that the fundamental resonances affecting the bulk modulus and mass density are monopolar and dipolar, while bianisotropy corresponds to monopolar-to-dipolar or dipolar-to-monopolar responses. This section discusses the details of the polarization process in terms of the scattering matrix in Eq. (5.1), which expresses the relations between even and odd incident and scattered fields. We first derive the scattered field generated from a small scatterer that satisfies the following constitutive relations [102]:

$$\begin{aligned} e &= B_0^{-1} p + M, \\ \boldsymbol{\pi} &= \rho_0 \mathbf{v} + \mathbf{D}, \end{aligned} \tag{B.1}$$

where e and $\boldsymbol{\pi}$ are the strain and momentum fields, respectively, and $M = -\frac{1}{V}\int \frac{\rho}{\rho_0} dV$ and $\mathbf{D} = -\frac{\partial_t}{V}\int \rho \mathbf{r} dV$ are monopolar and dipolar polarizations, respectively. Rewriting the acoustic wave equations with time harmonics $e^{-i\omega t}$ in terms of polarizations yields

$$\begin{aligned} \nabla p &= i\omega\left(\rho_0 \mathbf{v} + \mathbf{D}\right), \\ \nabla \cdot \mathbf{v} &= i\omega\left(B_0^{-1} p + M\right) \end{aligned}. \tag{B.2}$$

Therefore, the acoustic Helmholtz equation can then be written as

$$\left(\nabla^2 + k_0^{\,2}\right) p = i\omega\left(ik_0\rho_0 c_0 M + \nabla \cdot \mathbf{D}\right). \tag{B.3}$$

Since the Green's function of the 1D Helmholtz equation $\left(\nabla^2 + k_0^{\,2}\right) G\left(r - r'\right) = -\delta\left(r - r'\right)$ is given by $G\left(r - r'\right) = \frac{i}{2k_0} e^{ik_0|r-r'|}$, the scattered pressure fields p_M^s and p_D^s at $r = L/2 << 1$ induced by a monopole M and a dipole $\mathbf{D} = D\boldsymbol{x}$ located at the center ($r' = 0$) are written as

$$\begin{aligned} p_M^s &= \frac{i\omega\rho_0 c_0 ML}{2} e^{ik_0|L/2|}, \\ p_D^s &= \frac{i\omega \mathbf{D} \cdot \hat{\mathbf{r}} L}{2} e^{ik_0|L/2|}. \end{aligned} \tag{B.4}$$

The polarizations M and D can be written in terms of the normalized polarizability, by definition, as follows:

$$\begin{pmatrix} M \\ D \end{pmatrix} = \frac{1}{L}\begin{pmatrix} B_0^{-1}\alpha_{pp} & c_0^{-1}\alpha_{pv} \\ c_0^{-1}\alpha_{vp} & \rho_0\alpha_{vv} \end{pmatrix}\begin{pmatrix} p_{loc} \\ v_{loc} \end{pmatrix}, \tag{B.5}$$

where p_{loc} and v_{loc} are local fields representing the sum of the external fields exerted on the scatterers and the field induced by the geometry. When an incident wave is propagating in forward (+) or backward (–) direction, the scattered fields adjacent to the center are given by

$$p_+^r = \frac{i\omega L}{2}\left(\rho_0 c_0 M_+ + D_+\right), \quad p_+^t = \frac{i\omega L}{2}\left(\rho_0 c_0 M_+ - D_+\right) + p_{ext},$$

$$p_-^r = \frac{i\omega L}{2}\left(\rho_0 c_0 M_- - D_-\right), \quad p_-^t = \frac{i\omega L}{2}\left(\rho_0 c_0 M_- + D_-\right) + p_{ext}, \tag{B.6}$$

where the superscripts r and t denote the reflected and transmitted scattered fields, respectively. When the contributions of other unit cells to the local field are negligible, the local fields are determined simply by the external fields. Therefore, the scattering coefficients and polarizability can be written as

$$\begin{aligned} r_+ &= \frac{ik_0}{2}\left(\alpha_{pp} + \alpha_{pv} + \alpha_{vp} + \alpha_{vv}\right), \\ t_+ &= 1 + \frac{ik_0}{2}\left(\alpha_{pp} + \alpha_{pv} - \alpha_{vp} - \alpha_{vv}\right), \\ r_- &= \frac{ik_0}{2}\left(\alpha_{pp} - \alpha_{pv} - \alpha_{vp} + \alpha_{vv}\right), \\ t_- &= 1 + \frac{ik_0}{2}\left(\alpha_{pp} - \alpha_{pv} + \alpha_{vp} - \alpha_{vv}\right). \end{aligned} \tag{B.7}$$

The polarizability can then be described in terms of the forward and backward scattering parameters,

$$\begin{pmatrix} \alpha_{pp} & \alpha_{pv} \\ \alpha_{vp} & \alpha_{vv} \end{pmatrix} = \frac{1}{2ik_0} \begin{pmatrix} t_+ + t_- + r_+ + r_- - 2 & -t_+ + t_- + r_+ - r_- \\ t_+ - t_- + r_+ - r_- & -t_+ - t_- + r_+ - r_- - 2 \end{pmatrix}. \tag{B.8}$$

with the following relationship between the polarizability $\boldsymbol{\alpha}$ and the scattering matrix **S**:

$$\begin{pmatrix} \alpha_{pp} & \alpha_{pv} \\ \alpha_{vp} & \alpha_{vv} \end{pmatrix} = \frac{1}{ik_0} \begin{pmatrix} s_{ee} & s_{eo} \\ s_{oe} & s_{oo} \end{pmatrix}, \tag{B.9}$$

where the normalized polarizability is related to the effective wave parameters as follows:

$$\begin{pmatrix} B^{-1} & \xi \\ \zeta & \rho \end{pmatrix} = \begin{pmatrix} B_0^{-1}\left(1+\alpha_{pp}L^{-1}\right) & c_0^{-1}\alpha_{pv}L^{-1} \\ c_0^{-1}\alpha_{vp}L^{-1} & \rho_0\left(1+\alpha_{vv}L^{-1}\right) \end{pmatrix} . \tag{B.10}$$

B.2 Derivation of the maximum Willis coupling in a one-dimensional passive system

In this section, I develop a passivity condition for a one-dimensional bianisotropic system, following 2-D and 3-D cases by Quan et al. [86]. In a 1-D system, the incident and total pressure and velocity fields (propagating along the *x*-direction) can be written as

$$
\begin{aligned}
p_i &= \frac{a_e}{2}\left(e^{ikx}+e^{-ikx}\right)+\frac{a_o}{2}\left(e^{ikx}-e^{-ikx}\right),\\
\rho_0 c_0 v_i &= \frac{a_e}{2}\left(e^{ikx}-e^{-ikx}\right)+\frac{a_o}{2}\left(e^{ikx}+e^{-ikx}\right),\\
p_t &= \frac{a_e}{2}\left(e^{ikx}+e^{-ikx}\right)+\frac{a_o}{2}\left(e^{ikx}-e^{-ikx}\right)+\frac{b_e}{2}e^{ik|x|}+\frac{b_o}{2}\operatorname{sgn}(x)e^{ik|x|},\\
\rho_0 c_0 v_t &= \frac{a_e}{2}\left(e^{ikx}-e^{-ikx}\right)+\frac{a_o}{2}\left(e^{ikx}+e^{-ikx}\right)+\frac{b_e}{2}\operatorname{sgn}(x)e^{ik|x|}+\frac{b_o}{2}e^{ik|x|}.
\end{aligned}
\tag{B.11}
$$

The passivity of the system, meaning that the absorption power is always nonnegative, can be expressed as

$$
\frac{1}{2}\operatorname{Re}\int\left(p_i^{*}\mathbf{v}_i - p_t^{*}\mathbf{v}_t\right)\cdot d\mathbf{A} \geq 0. \tag{B.12}
$$

where the subscript i and t denote incident and total fields, respectively. This inequality can then be rewritten in terms of a_j and b_i as follows:

$$
\left(a_e^{*}b_e + a_o^{*}b_o + b_e^{*}a_e + b_o^{*}a_o + b_e b_e^{*} + b_o b_o^{*}\right) \leq 0. \tag{B.13}
$$

By rewriting Eq. (B.13) in the matrix form, the left-hand side can be simplified to $\mathbf{b}^\dagger\mathbf{b} + \mathbf{a}^\dagger\mathbf{b} + \mathbf{b}^\dagger\mathbf{a} = \mathbf{a}^\dagger(\mathbf{S}^\dagger\mathbf{S} + \mathbf{S} + \mathbf{S}^\dagger)\mathbf{a}$. Since the input $\mathbf{a}$ is an arbitrary vector, the Hermitian matrix $\mathbf{S}^\dagger\mathbf{S} + \mathbf{S} + \mathbf{S}^\dagger$ is a negative semidefinite matrix, which necessitates that the diagonal components must be nonpositive:

$$\begin{aligned} |s_{oe}|^2 + |1 + s_{ee}|^2 &\le 1, \\ |s_{eo}|^2 + |1 + s_{oo}|^2 &\le 1, \end{aligned} \tag{B.14}$$

or equivalently, in terms of the polarizability α,

$$\begin{aligned} |k_0\alpha_{vp}|^2 + |1 + ik_0\alpha_{pp}|^2 &\le 1, \\ |k_0\alpha_{pv}|^2 + |1 + ik_0\alpha_{vv}|^2 &\le 1. \end{aligned} \tag{B.15}$$

These results for a one-dimensional system are consistent with the two- and three-dimensional derivations are given by Ref. [86].

The scattering matrix $\mathbf{S}$ depends on the choice of the reference plane. In the main text, we define the reference plane that lies at the middle position between the two speakers S_1 and S_2 as an obvious choice. However, when we choose a reference plane that is shifted by $\Delta\varphi$ (in terms of phase), we have $r_f \to r_f e^{-2i\Delta\varphi}$ and $r_b \to r_b e^{2i\Delta\varphi}$. This corresponds to a unitary transformation of the matrix $\mathbf{S}$ as follows:

$$\mathbf{S}(\omega) \to \begin{pmatrix} \cos\Delta\varphi & i\sin\Delta\varphi \\ i\sin\Delta\varphi & \cos\Delta\varphi \end{pmatrix} \mathbf{S}(\omega) \begin{pmatrix} \cos\Delta\varphi & -i\sin\Delta\varphi \\ -i\sin\Delta\varphi & \cos\Delta\varphi \end{pmatrix}. \tag{B.16}$$

Such a unitary transformation will not change the eigenvalues of $\mathbf{S}^\dagger\mathbf{S} + \mathbf{S} + \mathbf{S}^\dagger$; therefore, the passivity condition is invariant against the choice of reference plane, as expected, and the reciprocity condition $s_{eo} + s_{oe} = 0$ is also invariant. Therefore, the lower bound is invariant with respect to a shift of the reference plane.

B.3 Derivation of the scattering matrix in the virtual meta-atom structure

In this section, we discuss the exact scattering process of our virtual meta-atom structure, focusing on the generation of the local fields. The speakers (S_1, S_2) and microphones (M_1, M_2) are located at ($-\Delta s/2$, $\Delta s/2$) and ($-\Delta m/2$, $\Delta m/2$), respectively, where both Δm and $\Delta s > 0$, and are assumed to be omnidirectional, detecting pressure fields and generating acoustic waves propagating along both sides. Then, the total pressure field in the steady-state is given by

$$p(x) = S_1 e^{ik_0|x+\Delta s/2|} + S_2 e^{ik_0|x-\Delta s/2|} + I(x), \tag{B.17}$$

where $I(x) = I_+ \exp(ik_0x) + I_- \exp(-ik_0x)$ is the incident field. The microphones detect these steady-state total fields, i.e., $M_1 = p(-\Delta m/2)$ and $M_2 = p(\Delta m/2)$. The reflection and transmission coefficients are derived by setting the incident field $I(x)$ to $I_0\exp(ik_0x)$ and $I_0\exp(-ik_0x)$ for forward and backward incidence, respectively:

$$r_\pm = \left(p_\pm(\mp L) - e^{-ik_0L}\right)e^{-ik_0L}, \quad t_\pm = p_\pm(\pm L)e^{-ik_0L}, \tag{B.18}$$

where L is an arbitrarily long far-field distance satisfying $L \gg \Delta s$ and Δm, which will not affect these coefficients. In our virtual meta-atom structure, where $\Delta s = \Delta m = \Delta$, the scattering coefficients are explicitly written as

$$
\begin{aligned}
r_+ &= \frac{\left(Q-Y_{11}\right)e^{-ik_0\Delta}-\left(Q+Y_{22}\right)e^{ik_0\Delta}-\left(Y_{12}+Y_{21}\right)}{-1+Y_{11}+Y_{22}-Q+\left(Y_{12}+Y_{21}\right)e^{ik_0\Delta}+Qe^{2ik_0\Delta}},\\
t_+ &= \frac{-1+2iY_{21}\sin\left(k_0\Delta\right)}{-1+Y_{11}+Y_{22}-Q+\left(Y_{12}+Y_{21}\right)e^{ik_0\Delta}+Qe^{2ik_0\Delta}},\\
r_- &= \frac{\left(Q-Y_{22}\right)e^{-ik_0\Delta}-\left(Q+Y_{11}\right)e^{ik_0\Delta}-\left(Y_{12}+Y_{21}\right)}{-1+Y_{11}+Y_{22}-Q+\left(Y_{12}+Y_{21}\right)e^{ik_0\Delta}+Qe^{2ik_0\Delta}},\\
t_- &= \frac{-1+2iY_{12}\sin\left(k_0\Delta\right)}{-1+Y_{11}+Y_{22}-Q+\left(Y_{12}+Y_{21}\right)e^{ik_0\Delta}+Qe^{2ik_0\Delta}}.
\end{aligned}
\tag{B.19}
$$

where $Q = Y_{11}Y_{22} - Y_{12}Y_{21}$. Thus, the elements of the scattering matrix **S** are

$$
\begin{aligned}
s_{ee} &= \frac{2\cos\left(k_0\Delta/2\right)^2\left(Y_{11}+Y_{12}+Y_{21}+Y_{22}+2Q\left(\mathrm{e}^{ik_0\Delta}-1\right)\right)}{-1+Y_{11}+Y_{22}-Q+\left(Y_{12}+Y_{21}\right)e^{ik\Delta}+Qe^{2ik_0\Delta}},\\
s_{eo} &= \frac{i\sin\left(k_0\Delta\right)\left(Y_{11}-Y_{12}+Y_{21}-Y_{22}\right)}{-1+Y_{11}+Y_{22}-Q+\left(Y_{12}+Y_{21}\right)e^{ik_0\Delta}+Qe^{2ik_0\Delta}},\\
s_{oe} &= \frac{i\sin\left(k_0\Delta\right)\left(-Y_{11}-Y_{12}+Y_{21}+Y_{22}\right)}{-1+Y_{11}+Y_{22}-Q+\left(Y_{12}+Y_{21}\right)e^{ik_0\Delta}+Qe^{2ik_0\Delta}},\\
s_{oo} &= \frac{-2\sin\left(k_0\Delta/2\right)^2\left(-Y_{11}+Y_{12}+Y_{21}-Y_{22}+2Q\left(\mathrm{e}^{ik_0\Delta}+1\right)\right)}{-1+Y_{11}+Y_{22}-Q+\left(Y_{12}+Y_{21}\right)e^{ik_0\Delta}+Qe^{2ik_0\Delta}}.
\end{aligned}
\tag{B.20}
$$

Equivalently, by applying $\mathbf{Y} = Y_{ee}\mathbf{Y}_{ee} + Y_{eo}\mathbf{Y}_{eo} + Y_{oe}\mathbf{Y}_{oe} + Y_{oo}\mathbf{Y}_{oo}$, one can rewrite Eq. (B.20) as

$$
\begin{aligned}
s_{ee} &= \frac{4\cos\left(k_0\Delta/2\right)^2\left(Y_{ee}+\left(e^{ik_0\Delta}-1\right)\left(Y_{ee}Y_{oo}-Y_{eo}Y_{oe}\right)\right)}{1-\left(1+e^{ik_0\Delta}\right)Y_{ee}-\left(1-e^{ik_0\Delta}\right)Y_{oo}+\left(1-e^{2ik_0\Delta}\right)\left(Y_{ee}Y_{oo}-Y_{eo}Y_{oe}\right)},\\
s_{eo} &= \frac{2i\sin\left(k_0\Delta\right)Y_{eo}}{1-\left(1+e^{ik_0\Delta}\right)Y_{ee}-\left(1-e^{ik_0\Delta}\right)Y_{oo}+\left(1-e^{2ik_0\Delta}\right)\left(Y_{ee}Y_{oo}-Y_{eo}Y_{oe}\right)},\\
s_{oe} &= \frac{-2i\sin\left(k_0\Delta\right)Y_{oe}}{1-\left(1+e^{ik_0\Delta}\right)Y_{ee}-\left(1-e^{ik_0\Delta}\right)Y_{oo}+\left(1-e^{2ik_0\Delta}\right)\left(Y_{ee}Y_{oo}-Y_{eo}Y_{oe}\right)},\\
s_{oo} &= \frac{-4\sin\left(k_0\Delta/2\right)^2\left(Y_{oo}-\left(e^{ik_0\Delta}+1\right)\left(Y_{ee}Y_{oo}-Y_{eo}Y_{oe}\right)\right)}{1-\left(1+e^{ik_0\Delta}\right)Y_{ee}-\left(1-e^{ik_0\Delta}\right)Y_{oo}+\left(1-e^{2ik_0\Delta}\right)\left(Y_{ee}Y_{oo}-Y_{eo}Y_{oe}\right)}.
\end{aligned}
\tag{B.21}
$$

It is noted that since $Y \ll 1$ in our case, the higher-order term $Y_{ee}Y_{oo} - Y_{eo}Y_{oe}$ is negligible, and the denominator can simply be 1. Therefore, the virtualized atom exclusively excites the corresponding scattering components s_{ij} as follows:

$$
\begin{aligned}
s_{ee} &= 4\cos\left(k_0\Delta/2\right)^2 Y_{ee},\\
s_{eo} &= 2i\sin\left(k_0\Delta\right)Y_{eo},\\
s_{oe} &= -2iY_0\sin\left(k_0\Delta\right)Y_{oe},\\
s_{oo} &= -4\sin\left(k_0\Delta/2\right)^2 Y_{oo}.
\end{aligned}
\tag{B.22}
$$

B.4 Causality conditions in the inverse design of the frequency dispersion

The virtual meta-atom concept can enable the design of wave parameters over a broad frequency domain by virtue of its arbitrary software-defined frequency dispersion. Here, we remark on the possible issue of causality when inversely engineering the dispersion. The wideband flat dispersion in Eqs. (5.10) and (5.11) can be used to design a broadband, near-zero index by designing $\mathbf{Y}(\omega) = Y_{ee}(\omega)\mathbf{e}_{ee} + Y_{oo}(\omega)\mathbf{e}_{oo}$ with

$$\begin{aligned} F_0(\omega) &= \frac{2\cos(k\Delta/2)^2 Y_{ee}(\omega)}{1-2e^{ik\Delta/2}\cos(k\Delta/2)Y_{ee}(\omega)} \\ &= -\frac{2\sin(k\Delta/2)^2 Y_{oo}(\omega)}{1+2ie^{ik\Delta/2}\sin(k\Delta/2)Y_{oo}(\omega)} \end{aligned} . \quad \text{(B.23)}$$

Then, the required time-domain functions for the coefficients $y_{ee}(t)$ and $y_{oo}(t)$ can be inversely designed from Y_{ee} and Y_{oo}, either analytically or numerically. Figures B.1a,c show the required time-domain functions for a wideband zero inverse bulk modulus and mass density, which are calculated from the discrete inverse Fourier transforms of $Y_{ee}(\omega)$ and $Y_{oo}(\omega)$. Since the inverse design incurs anti-causal components (red shaded regions), which cannot be achieved, the realized polarizability must necessarily differ from the initially designed frequency response. In Fig.B.1b,d, the effective inverse bulk modulus and mass density reconstructed from only the causal components (green shaded regions) are depicted, showing severe deformation from a flat dispersion. The discrepancy is more significant in the case of y_{oo} because sensing a dipole-like incident signal requires more time steps in practice.

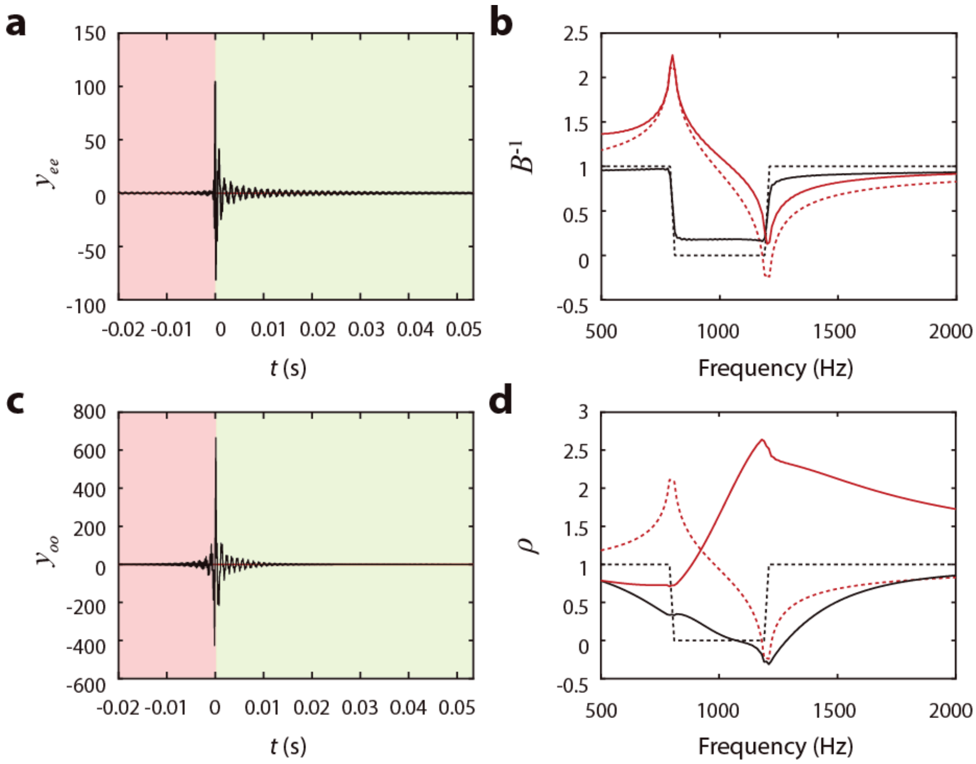

Figure B.1 | Causality analysis for the inverse bulk modulus and mass density. **a,** Required time-domain convolution function $y_{ee}(t)$ obtained from the discrete-time inverse Fourier transform of Y_{ee} for the wideband flat dispersion in Eq. (5.10). **b,** Numerically calculated inverse bulk modulus based on only the causal components of $y_{ee}(t)$, i.e., $y_{ee}(t)u(t)$, where $u(t)$ is the Heaviside step function. The real/imaginary parts are plotted as solid black/red lines, while the analytical results reconstructed from $y_{ee}(t)$ are plotted as dotted lines. **c,d** Same as **a,b** but for $y_{oo}(t)$ and the mass density.

Bibliography

[1] D. R. Smith, W. J. Padilla, D. Vier, S. C. Nemat-Nasser, and S. Schultz, Physical Review Letters **84**, 4184 (2000).

[2] J. B. Pendry, A. J. Holden, D. J. Robbins, and W. Stewart, IEEE transactions on microwave theory and techniques **47**, 2075 (1999).

[3] R. A. Shelby, D. R. Smith, and S. Schultz, Science **292**, 77 (2001).

[4] V. M. Shalaev, Nature Photonics **1**, 41 (2007).

[5] S. Linden, C. Enkrich, M. Wegener, J. Zhou, T. Koschny, and C. M. Soukoulis, Science **306**, 1351 (2004).

[6] V. M. Shalaev, W. Cai, U. K. Chettiar, H.-K. Yuan, A. K. Sarychev, V. P. Drachev, and A. V. Kildishev, Optics Letters **30**, 3356 (2005).

[7] P. Moitra, Y. Yang, Z. Anderson, I. I. Kravchenko, D. P. Briggs, and J. Valentine, Nature Photonics **7**, 791 (2013).

[8] Y. Li, S. Kita, P. Muñoz, O. Reshef, D. I. Vulis, M. Yin, M. Lončar, and E. Mazur, Nature Photonics **9**, 738 (2015).

[9] M. Choi *et al.*, Nature **470**, 369 (2011).

[10] Z. Liu, X. Zhang, Y. Mao, Y. Zhu, Z. Yang, C. T. Chan, and P. Sheng, Science **289**, 1734 (2000).

[11] J. Li and C. T. Chan, Physical Review E **70**, 055602 (2004).

[12] N. Fang, D. Xi, J. Xu, M. Ambati, W. Srituravanich, C. Sun, and X. Zhang, Nature Materials **5**, 452 (2006).

[13] Y. Ding, Z. Liu, C. Qiu, and J. Shi, Physical Review Letters **99**, 093904 (2007).

[14] S. H. Lee, C. M. Park, Y. M. Seo, Z. G. Wang, and C. K. Kim, Physics Letters A **373**, 4464 (2009).

[15] S. H. Lee, C. M. Park, Y. M. Seo, Z. G. Wang, and C. K. Kim, Physical Review Letters **104**, 054301 (2010).

[16] Z. Liang and J. Li, Physical Review Letters **108**, 114301 (2012).

[17] T. Brunet, A. Merlin, B. Mascaro, K. Zimny, J. Leng, O. Poncelet, C. Aristégui, and O. Mondain-Monval, Nature Materials **14**, 384 (2015).

[18] S. A. Cummer, J. Christensen, and A. Alù, Nature Reviews Materials **1**, 1 (2016).

[19] X. Hu, C. T. Chan, K.-M. Ho, and J. Zi, Physical Review Letters **106**, 174501 (2011).

[20] Y. Wu, Y. Lai, and Z.-Q. Zhang, Physical Review Letters **107**, 105506 (2011).

[21] S. Brûlé, E. Javelaud, S. Enoch, and S. Guenneau, Physical Review Letters **112**, 133901 (2014).

[22] P. Wang, F. Casadei, S. Shan, J. C. Weaver, and K. Bertoldi, Physical Review Letters **113**, 014301 (2014).

[23] R. Zhu, X. Liu, G. Hu, C. Sun, and G. Huang, Nature Communications **5**, 1 (2014).

[24] Y. Liu, X. Su, and C. Sun, Journal of the Mechanics and Physics of Solids **74**, 158 (2015).

[25] C. Luo, S. G. Johnson, J. Joannopoulos, and J. Pendry, Physical Review B **65**, 201104 (2002).

[26] E. Cubukcu, K. Aydin, E. Ozbay, S. Foteinopoulou, and C. M. Soukoulis, Nature **423**, 604 (2003).

[27] H. J. Lezec, J. A. Dionne, and H. A. Atwater, Science **316**, 430 (2007).

[28] Z. Liu, N. Fang, T.-J. Yen, and X. Zhang, Applied Physics Letters **83**, 5184 (2003).

[29] Z. Jacob, L. V. Alekseyev, and E. Narimanov, Optics Express **14**, 8247 (2006).

[30] M. B. Johnston, Nature Photonics **1**, 14 (2007).

[31] Z. Liu, H. Lee, Y. Xiong, C. Sun, and X. Zhang, Science **315**, 1686 (2007).

[32] I. I. Smolyaninov, Y.-J. Hung, and C. C. Davis, Science **315**, 1699

(2007).

[33] T. W. Ebbesen, H. J. Lezec, H. Ghaemi, T. Thio, and P. A. Wolff, Nature **391**, 667 (1998).

[34] T. Ergin, N. Stenger, P. Brenner, J. B. Pendry, and M. Wegener, Science **328**, 337 (2010).

[35] X. Chen, Y. Luo, J. Zhang, K. Jiang, J. B. Pendry, and S. Zhang, Nature Communications **2**, 1 (2011).

[36] R. Schittny, M. Kadic, T. Bückmann, and M. Wegener, Science **345**, 427 (2014).

[37] N. Yu, P. Genevet, M. A. Kats, F. Aieta, J.-P. Tetienne, F. Capasso, and Z. Gaburro, Science **334**, 333 (2011).

[38] X. Ni, A. V. Kildishev, and V. M. Shalaev, Nature Communications **4**, 1 (2013).

[39] D. Lin, P. Fan, E. Hasman, and M. L. Brongersma, Science **345**, 298 (2014).

[40] D. Dragoman and M. Dragoman, *Quantum-classical analogies* (Springer Science & Business Media, 2013).

[41] X. Zhang, Phys. Rev. Lett. **100**, 113903 (2008).

[42] K. Shandarova, C. E. Rüter, D. Kip, K. G. Makris, D. N. Christodoulides, O. Peleg, and M. Segev, Phys. Rev. Lett. **102**, 123905 (2009).

[43] A. Kavokin, G. Malpuech, and M. Glazov, Phys. Rev. Lett. **95**, 136601 (2005).

[44] S. Raghu and F. D. M. Haldane, Phys. Rev. A **78**, 033834 (2008).

[45] L. Lu, J. D. Joannopoulos, and M. Soljačić, Nat. Photonics **8**, 821 (2014).

[46] C. He, X. Ni, H. Ge, X.-C. Sun, Y.-B. Chen, M.-H. Lu, X.-P. Liu, and Y.-F. Chen, Nat. Phys. **12**, 1124 (2016).

[47] C. E. Rüter, K. G. Makris, R. El-Ganainy, D. N. Christodoulides, M. Segev, and D. Kip, Nat. Phys. **6**, 192 (2010).

[48] T. Schwartz, G. Bartal, S. Fishman, and M. Segev, Nature **446**, 52 (2007).

[49] M. Ben Dahan, E. Peik, J. Reichel, Y. Castin, and C. Salomon, Phys. Rev. Lett. **76**, 4508 (1996).

[50] H. Sanchis-Alepuz, Y. A. Kosevich, and J. Sánchez-Dehesa, Phys. Rev. Lett. **98**, 134301 (2007).

[51] M.-A. Miri, M. Heinrich, R. El-Ganainy, and D. N. Christodoulides, Phys. Rev. Lett. **110**, 233902 (2013).

[52] M.-A. Miri, M. Heinrich, and D. N. Christodoulides, Phys. Rev. A **87**, 043819 (2013).

[53] M. Heinrich, M.-A. Miri, S. Stützer, R. El-Ganainy, S. Nolte, A. Szameit, and D. N. Christodoulides, Nat. Commun. **5**, 3698 (2014).

[54] S. Yu, X. Piao, J. Hong, and N. Park, Nat. Commun. **6**, 8269 (2015).

[55] S. Yu, X. Piao, and N. Park, Phys. Rev. Appl. **8**, 054010 (2017).

[56] D. Schurig, J. J. Mock, B. Justice, S. A. Cummer, J. B. Pendry, A. F. Starr, and D. R. Smith, Science **314**, 977 (2006).

[57] S. Zhang, C. Xia, and N. Fang, Physical Review Letters **106**, 024301 (2011).

[58] S. Xiao, V. P. Drachev, A. V. Kildishev, X. Ni, U. K. Chettiar, H.-K. Yuan, and V. M. Shalaev, Nature **466**, 735 (2010).

[59] O. Hess, J. B. Pendry, S. A. Maier, R. F. Oulton, J. M. Hamm, and K. L. Tsakmakidis, Nature Materials **11**, 573 (2012).

[60] J.-Y. Ou, E. Plum, J. Zhang, and N. I. Zheludev, Nature Nanotechnology **8**, 252 (2013).

[61] M. Manjappa, P. Pitchappa, N. Singh, N. Wang, N. I. Zheludev, C. Lee, and R. Singh, Nature Communications **9**, 1 (2018).

[62] C. Della Giovampaola and N. Engheta, Nature Materials **13**, 1115 (2014).

[63] P. Celli, W. Zhang, and S. Gonella, Physical Review Applied **9**, 014014 (2018).

[64] J. P. Xia, D. Jia, H. X. Sun, S. Q. Yuan, Y. Ge, Q. R. Si, and X. J. Liu, Advanced Materials **30**, 1805002 (2018).

[65] J. B. Pendry, D. Schurig, and D. R. Smith, Science **312**, 1780 (2006).

[66] B.-I. Popa, L. Zigoneanu, and S. A. Cummer, Physical Review B **88**, 024303 (2013).

[67] R. Fleury, D. Sounas, and A. Alu, Nature Communications **6**, 1 (2015).

[68] B.-I. Popa, Y. Zhai, and H.-S. Kwon, Nature communications **9**, 1 (2018).

[69] Y. Zhai, H.-S. Kwon, and B.-I. Popa, Physical Review B **99**, 220301 (2019).

[70] C. Luo, Y. Song, C. Zhao, S. Thirumalai, I. Ladner, M. A. Cullinan, and J. B. Hopkins, Materials Horizons **7**, 229 (2020).

[71] G. W. Milton and N.-A. P. Nicorovici, Proceedings of the Royal Society A: Mathematical, Physical and Engineering Sciences **462**, 3027 (2006).

[72] S. A. Cummer and D. Schurig, New Journal of Physics **9**, 45 (2007).

[73] S. A. Cummer, B.-I. Popa, D. Schurig, D. R. Smith, J. Pendry, M. Rahm, and A. Starr, Phys. Rev. Lett. **100**, 024301 (2008).

[74] H. Chen and C. Chan, Applied Physics Letters **91**, 183518 (2007).

[75] V. M. García-Chocano, J. Christensen, and J. Sánchez-Dehesa, Physical Review Letters **112**, 144301 (2014).

[76] M.-H. Lu, X.-K. Liu, L. Feng, J. Li, C.-P. Huang, Y.-F. Chen, Y.-Y. Zhu, S.-N. Zhu, and N.-B. Ming, Physical Review Letters **99**, 174301 (2007).

[77] I. V. Lindell, A. H. Sihvola, and A. J. Viitanen, Microwave and Optical Technology Letters **5**, 79 (1992).

[78] A. Sihvola, A. Viitanen, I. Lindell, and S. Tretyakov, Norwood, MA, USA: Artech House (1994).

[79] J. R. Willis, Wave Motion **3**, 1 (1981).

[80] S. Koo, C. Cho, J.-h. Jeong, and N. Park, Nature Communications **7**, 1 (2016).

[81] M. B. Muhlestein, C. F. Sieck, P. S. Wilson, and M. R. Haberman,

Nature communications **8**, 1 (2017).

[82] A. Melnikov, Y. K. Chiang, L. Quan, S. Oberst, A. Alù, S. Marburg, and D. Powell, Nature Communications **10**, 1 (2019).

[83] L. Quan, D. L. Sounas, and A. Alù, Physical Review Letters **123**, 064301 (2019).

[84] R. Fleury, D. L. Sounas, C. F. Sieck, M. R. Haberman, and A. Alù, Science **343**, 516 (2014).

[85] C. Shen, X. Zhu, J. Li, and S. A. Cummer, Physical Review B **100**, 054302 (2019).

[86] L. Quan, Y. Ra'di, D. L. Sounas, and A. Alù, Physical Review Letters **120**, 254301 (2018).

[87] J. Li, C. Shen, A. Díaz-Rubio, S. A. Tretyakov, and S. A. Cummer, Nature Communications **9**, 1342 (2018).

[88] S. Zhang, W. Fan, K. Malloy, S. Brueck, N. Panoiu, and R. Osgood, Optics Express **13**, 4922 (2005).

[89] A. Ahmadi and H. Mosallaei, Physical Review B **77**, 045104 (2008).

[90] J.-Y. Ou, E. Plum, L. Jiang, and N. I. Zheludev, Nano Letters **11**, 2142 (2011).

[91] A. Alu, Physical Review B **84**, 075153 (2011).

[92] Y. Wu, Y. Lai, and Z.-Q. Zhang, Physical Review B **76**, 205313 (2007).

[93] X. Huang, Y. Lai, Z. H. Hang, H. Zheng, and C. Chan, Nature Materials **10**, 582 (2011).

[94] C. Pfeiffer and A. Grbic, Physical Review Letters **110**, 197401 (2013).

[95] C. Goffaux, J. Sánchez-Dehesa, A. L. Yeyati, P. Lambin, A. Khelif, J. Vasseur, and B. Djafari-Rouhani, Physical Review Letters **88**, 225502 (2002).

[96] A. Shaltout, A. Kildishev, and V. Shalaev, Optical Materials Express **5**, 2459 (2015).

[97] K. Fang, Z. Yu, and S. Fan, Nature Photonics **6**, 782 (2012).

[98] M. C. Rechtsman, J. M. Zeuner, Y. Plotnik, Y. Lumer, D. Podolsky, F.

Dreisow, S. Nolte, M. Segev, and A. Szameit, Nature **496**, 196 (2013).

[99] Z. Turker, S. Tombuloglu, and C. Yuce, Physics Letters A **382**, 2013 (2018).

[100] C. Poli, M. Bellec, U. Kuhl, F. Mortessagne, and H. Schomerus, Nature communications **6**, 1 (2015).

[101] X. Zhu, H. Ramezani, C. Shi, J. Zhu, and X. Zhang, Physical Review X **4**, 031042 (2014).

[102] L. E. Kinsler, A. R. Frey, A. B. Coppens, and J. V. Sanders, *Fundamentals of acoustics* (Wiley, New York, 1999).

Publication and Conference Presentation

Journal Papers

1. **C. Cho**†, X. Wen†, N. Park, and J. Li, "Acoustic Willis metamaterials beyond the passivity and reciprocity bound", under review.
2. **C. Cho**, S. Yu, and N. Park, "Elastic Hamiltonians for quantum-analog applications", *Physical Review B* **101**, 13, 134107 (2020).
3. **C. Cho**†, X. Wen†, N. Park, and J. Li, "Digitally Virtualized atoms for acoustic metamaterials", *Nature Communications* **11**, 251 (2020).
4. D. Lee†, J. Mun†, **C. Cho**, N. Park, and J. Rho, "Retrieving continuously-varying effective properties of non-resonant acoustic metamaterials", *Applied Physics Express* **12**, 5, 052008 (2019).
5. D. Lee†, **C. Cho**†, J. Mun, N. Park, and J. Rho, "Demonstration of steering acoustic waves by generalized Eaton lens", *Applied Physics Letters* **113**, 16, 161904 (2018).
6. S. Koo, **C. Cho**, J. Jeong, and N. Park, "Acoustic omni meta-atom for decoupled access to all octants of a wave parameter space", *Nature Communications* **7**, 13012 (2016).

† indicates equal contributors.

Conference Presentations

1. **C. Cho**, S. Yu, and N. Park, “Elastic mode converter based on supersymmetric ladders”, META 2019, Lisbon, Portugal (2019).
2. **C. Cho**, N. Park, and J. Li, “Huygens’ shells for non-reciprocal communication”, PIERS 2019, Rome, Italy (2019).
3. S. Yu, X. Piao, **C. Cho**, and N. Park, “Phase manipulation of constant-intensity waves in disordered optical structures”, Metamaterials'2018, Espoo, Finland (2018).
4. D. Lee, **C. Cho**, N. Park, and J. Rho, “Demonstration of steering acoustic waves by generalized Eaton lens”, Metamaterials'2018, Espoo, Finland (2018).
5. S. Yu, X. Piao, **C. Cho**, and N. Park, “Symmetries in optical Hamiltonians for isospectrality”, CLEO-PR 2018, Workshop 6, Hong Kong (2018).
6. S. Yu, X. Piao, **C. Cho**, and N. Park, “Multimodal parity conversion in supersymmetric optical potentials for controlling random waves”, CLEO 2018, JW2A.110, San Jose, CA, USA (2018).
7. S. Yu, X. Piao, **C. Cho**, and N. Park, “Isospectral transformations for disordered photonics”, META 2017, 2A11, Songdo, Korea (2017).
8. S. Yu, X. Piao, **C. Cho**, and N. Park, “Lorentz-force picture for controlling optical polarizations in non-Hermitian potentials”, META 2017, 1A28, Songdo, Korea (2017).
9. S. Koo, **C. Cho**, J. Jeong, and N. Park, “Acoustic omni meta-atom for decoupled access to all octants of a wave parameter space”, META 2017,

1A23, Songdo, Korea (2017).

10. **C. Cho** and N. Park, “Bianisotropic acoustic metasurfaces for independent control of reflection and transmission wave”, Acoustics ’17 Boston, 3pPAc, Boston, USA (2017).

11. J. Pang, **C. Cho**, and N. Park, “Sub-Wavelength Bi-anisotropic Acoustic Metamaterial for extreme impedance mismatch control”, A3 Metamaterials Forum, Shanghai, China (2017).

12. **C. Cho**, J. Pang, S. Koo, and N. Park, “Extension of Generalized Snell's Law: Bianisotropic Metasurfaces for independent control of reflection and transmission wavefronts”, A3 Metamaterials Forum, I-1, Shanghai, China (2017).

13. S. Yu, X. Piao, **C. Cho**, and N. Park, “Collective Resonances in Subwavelength Metadisorder Structures”, SPP8, P-07-43, Taipei, Taiwan (2017).

14. S. Yu, X. Piao, **C. Cho**, and N. Park, “Metadisorder coupled systems for functional wave transport”, iSPN 2017, IN-80, Dalian, China (2017).

15. S. Yu, X. Piao, **C. Cho**, and N. Park, “Interdimensional wave transport based on optical isospectrality”, iSPN 2017, IN-59, Dalian, China (2017).

16. **C. Cho**, S. Koo, and N. Park, “Beam Steering and Focusing by Impedance-matched Acoustic Meta-Surface”, 4th Korea-Japan Metamaterials Forum 2014, P8, Osaka, Japan (2014).

국문 초록

최근 20 년간 메타 물질은 파동제어 기법에 있어 혁신을 가져왔다. 메타 물질은 단위 구조체에서의 공진 모드를 인공적으로 설계함으로써 자연 물질이 나타낼 수 없는 파동 물성의 구현을 가능케 한다. 모든 파동 현상은 파동이 전파되는 공간의 파동 물성 분포에 의해 결정되므로, 전자기파, 음파, 그리고 탄성파 등, 다양한 파동 영역에서 파동 물성의 완전한 제어는 음굴절, 클로킹과 같은 많은 흥미로운 현상을 가능하게 한다. 이와 같이 파동 물성의 극한적 제어를 위한 다양한 구조체가 제시되어 왔음에도 불구하고 기존의 메타 물질 설계 방식은 다음과 같은 근본적인 한계점을 갖는다.

대부분의 실용적인 목적의 메타 물질 응용을 위해서는 메타 물질의 재구성 가능성을 필요로 한다. 이를 위해 각 파동 물성에 대한 독립적인 제어가 가능한 구조체가 재구성 가능성에 적합한 구조로써 제시되어 왔으나, 파동 매개 변수의 분리가 가능한 대부분의 메타 물질은 하나의 기본 공진 모드를 제어하는 하위 구조의 조합으로 구성되므로, 하향식 제어를 제공하는 통합된 플랫폼에 대한 연구를 필요로 한다. 특히, 재구성 가능한 메타 물질의 경우 구성 매개 변수를 조정하는 능력은 메타 물질과 결합된 물리적 구조를 수정하는 능력에 따라 달라지므로, 실시간 동작에 있어 재구성 가능성에서 제어 가능한 영역의 범위에 근본적인 한계를 갖

는다. 따라서 유연한 제어를 달성하고 극한 물성을 구현하기 위한 방법에 대한 연구가 필요하다.

본 학위 논문에서는 기존의 한계를 극복하고 결정론적으로 설계 가능한 파동 물성을 구현하기 위한 음향 메타 물질의 하향식 설계에 대해 분석한다. 기본 공진모드의 디커플링 원리를 기반으로, 파동 매개 변수를 독립적으로 제어 할 수 있는 음향 메타 물질 단위 구조체를 제안한다. 또한, 메타 물질의 물리적 구조에 의한 경계를 벗어나 디지털 신호 처리 기술을 기반으로 인공적인 분극을 구현하는 가상화 메타 물질의 개념을 제안한다. 가상화 메타 물질은 재구성 가능한 메타 물질로써, 가능한 모든 복소 파동 매개 변수를 분리 제어 할 수 있을 뿐만 아니라 극한 파동 물성을 구현할 수 있다. 본 연구는 모든 파동 물성을 독립적으로 구현할 뿐만 아니라, 설계 가능한 주파수 분산 특성을 실현함으로써 메타 물질 설계에 돌파구를 제공하고 음향 메타 물질의 전체 기능을 실현할 수 있는 유연한 플랫폼을 제공할 것으로 기대한다.

주요어 : 메타물질, 음향학, 쌍이방성, 능동 메타물질, 파동 역학

학번 : 2013-20890